PRECOMBUSTION CHAMBER PERFORMANCE AND EMISSIONS STUDIES ON A LARGE-BORE SINGLE CYLINDER NATURAL GAS ENGINE

A Thesis

by

KYLE BLAIR WARD

Submitted to the Office of Graduate and Professional Studies of
Texas A&M University
in partial fulfillment of the requirements for the degree of

MASTER OF SCIENCE

Chair of Committee,	Timothy J. Jacobs
Committee Members,	Eric L. Petersen
	Chad V. Mashuga
Head of Department,	Andreas A. Polycarpou

May 2021

Major Subject: Mechanical Engineering

ABSTRACT

Natural gas accounts for 32 percent of the United States' total energy consumption [1], and as emissions regulations become more stringent, the need to reduce harmful emissions produced by natural gas engines has become increasingly important. One solution is to burn air-fuel mixtures in open chamber spark ignition with very lean air-fuel ratios, which reduces oxides of nitrogen (NOx) emissions. However, this process dramatically increases carbon monoxide (CO) and hydrocarbon (HC) emissions. To combat harmful emission, a precombustion chamber (PCC) can be introduced into the system. A PCC is a small chamber, about 1 to 2 percent of the main chamber's clearance volume, that ignites a near stoichiometric air-fuel mixture and ejects an explosive jet into the main chamber. As a result, approximately one million times greater ignition energy is released compared to a normal spark plug [2] [3] [4]. Combustion stabilizes and in-cylinder temperatures are reduced, which reduces CO, HC, and NOx emissions.

This study provides performance and emissions data on three PCCs supplied by Cooper Machinery Services on an Ajax E-565 natural gas engine. A spark-ignited precombustion chamber for engine bore sizes of 10.5 inches up to 13.25 inches was tested to obtain performance and emissions data. Two other PCCs, Eco-Jets, were tested for the first time on an Ajax E-565 engine to obtain performance and emissions data. The novel results were analyzed, and further research and design opportunities were provided with a goal to reduce overall emissions, improve combustion stability, and improve engine performance.

DEDICATION

For my papou (grandpa), Steve Meimetis, who taught me to work hard at everything I set my mind to. Papou immigrated from Greece when he was 18 years old and worked as a mechanic in Arizona and then California. Eventually, he bought the very shop he worked at, had a beautiful family in the United States, and spent his days at his property in the Southern California mountains. While I was growing up, he taught me how to drive with a stick shift, how to be creative and inventive, and how to work with my hands and not be afraid to get them dirty. His stories, knowledge, and love have inspired me more than anyone else, and I would not be the person or engineer that I am without his influence.

I love you, Papou.

ACKNOWLEDGEMENTS

I would first like to thank my committee chair and advisor, Dr. Timothy Jacobs, for his continuous guidance and support. One year before I started attending Texas A&M University, I visited Dr. Jacobs's Advanced Engine Research Lab (AERL) and he was so generous in scheduling a lab visit with AERL graduate students. I learned about the wonderful research projects on the diesel engines and natural gas engine, and knew I needed to join his lab at Texas A&M. Once I started classes in the fall of 2019, Dr. Jacobs provided the guidance, knowledge, and autonomy I needed to be successful at Texas A&M. I have learned more than I could have possibly imagined and would not have had such an incredible experience without Dr. Jacobs.

I would also like to thank my peers in AERL, specifically Tim Kroeger and Abdullah Bajwa, for their expertise and guidance. Abdullah and Timothy met with me on several occasions to teach the principles behind the Ajax E-565 engine and Tim assisted in conducting the prechamber experiments, which I could not have done by myself. With their support and knowledge, I have developed into a more confident researcher and engineer.

This study would not have been possible without Cooper Machinery Services, who provided the precombustion chambers, parts, and knowledge necessary for successful experimentation. Lastly, I would like to thank all of my committee members, Dr. Jacobs, Dr. Mashuga, Dr. Petersen, and Dr. Polycarpou, for their continuous support and interest in this study.

CONTRIBUTORS AND FUNDING SOURCES

Contributors

This study was supervised by a thesis committee consisting of Dr. Timothy Jacobs, Dr. Eric Petersen, and Dr. Andreas Polycarpou of the Department of Mechanical Engineering and Dr. Chad Mashuga of the Department of Chemical Engineering. Installation of new plumbing and parts for fueling the precombustion chambers was completed by SSC Services for Education.

All other work conducted for this thesis was completed independently by the student.

Funding Sources

Precombustion chambers, a fuel filter, and fuel regulators required for successful experimentation were provided by Cooper Machinery Services. Additional parts and services were funded by AERL.

NOMENCLATURE

AERL	Advanced Engine Research Lab
OEM	Original Equipment Manufacturer
TDC	Top Dead Center
BDC	Bottom Dead Center
SI	Spark-Ignited
NO_x	Oxides of Nitrogen
HC	Unburned or Partially Burned Hydrocarbons
THC	Total Hydrocarbons
CO	Carbon Monoxide
CO_2	Carbon Dioxide
NO	Nitric Oxide
BSTHC	Brake Specific Total Hydrocarbons
BSCO	Brake Specific Carbon Monoxide
$BSCO_2$	Brake Specific Carbon Dioxide
$BSNO_x$	Brake Specific Oxides of Nitrogen
PCC	Precombustion Chamber
MCC	Main Combustion Chamber
OC	Open Chamber
SIP / P1	Screw-In-Prechamber
P2	#10-GMVH-13-10 Eco-Jet Prechamber

P3	GMVH-13-11 Eco-Jet Prechamber
DAQ	Data Acquisition System
NDIR	Non-Dispersive Infrared Absorption
NS	Nominal Spark Timing
AS	Advanced Spark Timing
BTDC	Before Top Dead Center
ATDC	After Top Dead Center
ϕ	Equivalence Ratio
IMEP	Indicated Mean Effective Pressure
COV_{IMEP}	Coefficient of Variation In IMEP
LoPP	Location of Peak Pressure
m_{fuel}/cycle	Mass of Fuel Per Cycle
CA-50	Crank Angle at Which 50% of Combustion Heat is Released
$\eta_{f,i}$	Indicated Fuel Conversion Efficiency
η_c	Combustion Efficiency
$\eta_{f,b}$	Brake Fuel Conversion Efficiency
$\eta_{t,b}$	Brake Thermal Efficiency
ROHR	Rate of Heat Release
MFB	Mass Fraction Burned
EOC	End of Combustion
EPO	Exhaust Port Opening

TABLE OF CONTENTS

Page

LIST OF FIGURES

Page

LIST OF TABLES

Page

1. INTRODUCTION

1.1. Motivation

Greenhouse gas emissions are rising globally due to an increased use of fossil fuels. Globally, CO_2 emissions rose 3% from 2000 to 2013, 0.4% from 2013 to 2016, 1.6% in 2017, and then 2.7% in 2018 alone (the United States being the second largest contributor to fossil CO_2 emissions) [5]. Figure 1 shows an increasing trend in global fossil CO_2 emissions, with the largest contribution to rising CO_2 levels from fossil fuel combustion (i.e. internal combustion engines) [6]. To help combat rising CO_2 levels, natural gas is an attractive fuel source due to its comparatively low CO_2 output [7].

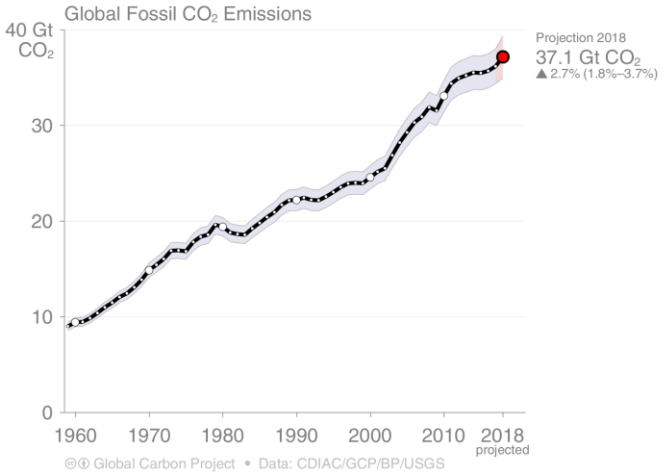

Figure 1: Global fossil CO_2 emissions. Reprinted from [5].

Natural gas accounts for 32% of the United States' total energy consumption (Figure 2) [1], and as emissions regulations become more stringent, the need to reduce harmful emissions produced by natural gas engines has become increasingly important.

Due to high NO_x output from spark-ignited natural gas two-stroke engines, operating them with a lean fuel-air mixture can help reduce NO_x levels to meet emissions regulations. However, lean engine operation dramatically increases carbon monoxide (CO) and hydrocarbon (HC) emissions. Some methods to increase the engine lean limit, while attempting to keep greenhouse gas emissions low, include laser induced ignition, diesel pilot ignition, and prechamber (PCC) ignition [7].

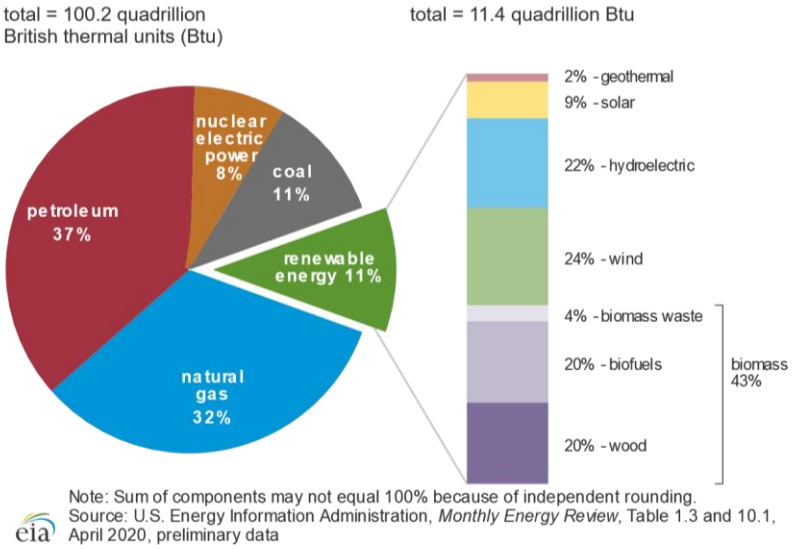

Figure 2: U.S. primary energy consumption by energy source in 2019. Reprinted from [1].

The present study investigates the effects of three PCCs, supplied by Cooper Machinery Services, on an Ajax E-565 natural gas engine. Ajax Iron Works began producing steam engines in 1877 and added gas engines in 1895, making Ajax the oldest continuous engine line in the U.S. used for the oil and gas industry. In 1959, Cooper Machinery Services became the original equipment manufacturer (OEM) of Ajax engines

and has since continued Ajax's strong reputation of reliability and efficiency. With Ajax engines still prominent in the oil and gas industry, this study aims to provide performance and emissions data on a PCC-configured Ajax E-565 natural gas engine to aid in the design and development of PCCs for use in two-stroke natural gas engines.

1.2. Background

1.2.1. Two-Stroke Engine Cycle

The engine used in this study is the Ajax E-565, a two-stroke, single cylinder, and spark-ignited natural gas engine. A two-stroke engine completes the power cycle (intake, compression, combustion, and exhaust) in two strokes. At the start of the cycle, the piston compresses the fuel-air mixture with the cylinder closed during the upstroke. While the piston is completing its upstroke, a vacuum is created in the stuffing box behind the piston, charging the fuel-air mixture for the next cycle [8]. With a direct injection system, there is only air in the stuffing box. Figure 3 shows the fuel-air mixture being compressed in a two-stroke Ajax E-565 engine.

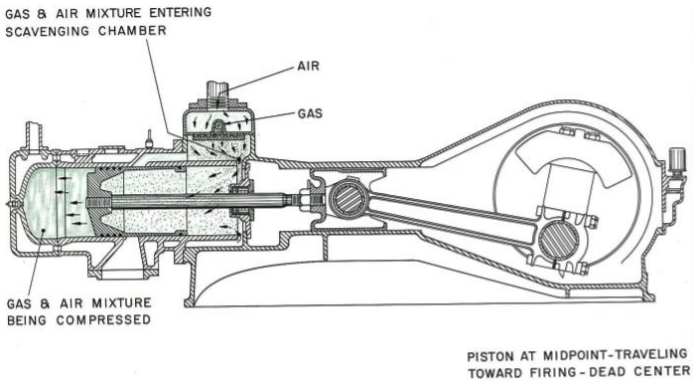

Figure 3: Ajax E-565 compression stroke. Reprinted from [9].

Once the piston approaches top dead center (TDC), a spark ignites the mixture, combustion increases the cylinder pressure, and this pressure forces the piston down during expansion. During the downstroke, the exhaust ports open first in order to release the complete, and incomplete, combustion products during blow-down. As combustion products are being exhausted, the charged fuel-air mixture in the stuffing box continues to be compressed by the piston. Within the same downstroke, the intake ports open shortly after and allows the fresh fuel-air mixture to rush in as the chamber's pressure decreases to a lower pressure than the scavenging chamber. As the fresh fuel-air mixture enters, the mixture helps push the remaining exhaust products out of the exhaust ports during the scavenging process (Figure 4) [8]. With a direct injection system, the exhaust products are almost all ejected by the time the direct injection valve opens and allows fuel flow.

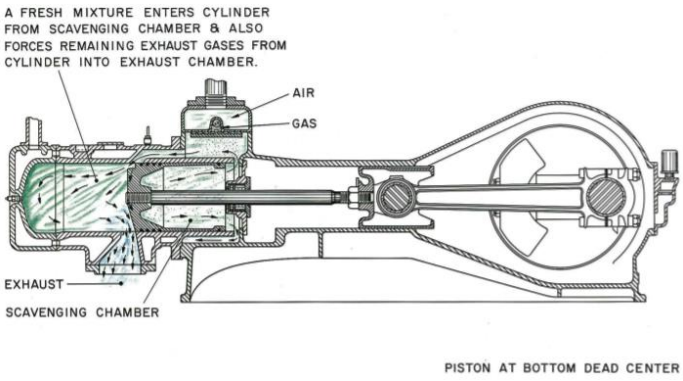

Figure 4: Ajax E-565 expansion stroke. Reprinted from [9].

The scavenging process results in a loss of some fresh charge through the exhaust ports, but the simple design of a two-stroke engine allows for greater reliability. The scavenging arrangement of the engine used in this study is classified as cross-scavenged,

but loop-scavenged and uniflow-scavenged configurations can also be used [8]. The cross-scavenged system has the intake and exhaust ports along the cylinder wall, which opens the exhaust port first, and then the intake port, as the piston approaches bottom dead center (BDC).

Two-stroke engines are simpler than four-stroke engines, as two-stroke engines do not have valves or a camshaft. Thus, fewer parts are susceptible to wearing down during operation. The use of a single cylinder further simplifies and strengthens the design, and allows for the use of thermo-syphon circulation, which removes the need of a water pump to keep the engine cool. Lastly, port scavenging in the two-stroke cycle provides greater fuel economy as fewer cubic feet of gas per horsepower-hour are used, and smoother flows of power are provided by slower speeds at which power is rated and a heavy flywheel [9].

1.2.2. Precombustion Chambers

A PCC can be introduced to a natural gas engine setup to combat harmful emissions. A PCC is a small chamber, about 1% to 2% of the main chamber's clearance volume, that ignites a near stoichiometric air-fuel mixture and ejects an explosive jet into the main chamber. As a result, approximately one million times greater ignition energy is released compared to a normal spark plug [2] [3] [4]. PCCs introduce a fuel-rich mixture into the main chamber, where the PCC experiences extremely high temperatures and contributes to the majority of the NO_x output now that NO_x production by the MCC is significantly reduced. However, combustion stabilizes at lean operating conditions in the main chamber as the PCC introduces extra energy to make the mixture easier to ignite,

and in-cylinder temperatures are reduced surrounding the mixture injected by the PCC, which reduces overall CO, HC, and NO_x emissions.

This study tested three PCCs supplied by Cooper Machinery Services: a standard screw-in-prechamber (SIP) and two Eco-Jet PCCs, all with varying sizes and nozzle outlets. The volume, length, and nozzle of a PCC directly affects the performance and emissions of the engine, with smaller volumes usually decreasing emission concentrations [10]. Additionally, a manual check valve was used on each PCC to prevent backflow. PCC design and contribution to emissions are discussed in greater detail in section *2. Literature Review*.

For this study, a new fuel line system was designed and installed on the Ajax E-565 to provide natural gas fuel to the PCC during operation under nominal and advanced spark timing. Data was collected using sensors, such as piezoelectric transducers and thermocouples, then post-processed. The post-processed data was used to calculate engine performance parameters to investigate the effects of the PCCs on the two-stroke, natural gas engine. In addition to engine performance parameters, brake specific emissions were analyzed to compare the differences in pollutants exhausted as a result of operating the engine with the different PCCs. The results are outlined and discussed in section *4. Results and Discussion*.

1.3. Objective

The first objective of this study was to install the new fuel line system to the Ajax E-565 to provide the Advanced Engine Research Lab (AERL) with PCC testing

capabilities. The fuel line integrated AERL's ethane blending system for future research related to the effects of fuel composition on PCC performance and emissions. Next, this study aimed to provide engine performance parameters and brake specific emission results to thoroughly investigate how each PCC influenced the Ajax E-565 engine. After investigating the results, the next objectives were to determine optimal pressures entering the PCC and main chamber, explore changes due to advanced ignition timing, and increase engine load to stabilize combustion and synthesize the data.

Lastly, this study concluded with design opportunities for Cooper Machinery Services and future research opportunities for AERL that may enhance PCC performance and emissions results based on experimental data and a literature review. Continuing to improve PCC operation on natural gas engines will aid in reducing global greenhouse gases and harmful pollutant emissions. As global natural gas usage continues to increase and emissions standards becomes more stringent, the need to improve internal combustion engines powered by natural gas becomes more relevant.

2. LITERATURE REVIEW

2.1. Emission Formation in Spark-Ignited Engines

Natural gas accounts for 32% of the United States' total energy consumption [1] and emits oxides of nitrogen (NO_x), unburned hydrocarbons (HC), carbon monoxide (CO), and carbon dioxide (CO_2). In spark-ignited natural gas engines, leaner fuel-air mixtures tend to reduce emissions until misfires occur due to poor combustion quality (i.e. the air-fuel mixture contains too much oxygen). Figure 5 shows how nitric oxide (NO), HC, and CO emissions vary with air-fuel ratio and fuel-air equivalence ratio. Note that Figure 5 is for gasoline engines, with the top horizonal axis reflecting gasoline's stoichiometric ratio; however, the behavior of NO, HC, and CO production with changing air-fuel ratio is the same for natural gas engines.

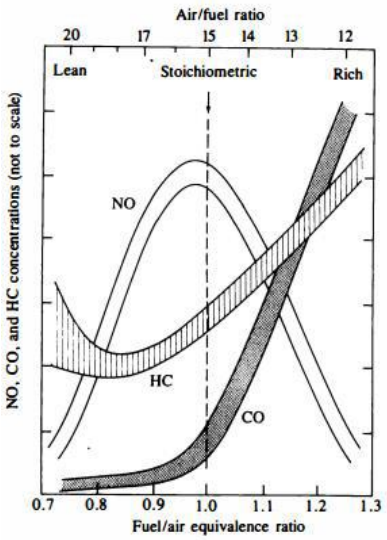

Figure 5: Variation in spark-ignition engine exhaust pollutants. Reprinted from [8].

Fuel-air equivalence ratio, ϕ, is the ratio of the engine's actual fuel-air ratio to the stoichiometric fuel-air ratio. When ϕ is less than one, combustion is lean, when ϕ is greater than one, the fuel-air mixture is rich with incomplete combustion due to excess fuel [11]. This phenomenon is further evidenced when observing air-fuel ratio in Figure 5. When ϕ is less than one, the air-fuel ratio rises with increasing air content, thus becoming leaner. NO emissions are maximized slightly lean of stoichiometric, where combustion temperature is highest. When ϕ decreases further, the NO, HC, and CO pollutants decrease until misfire occurs, at which point the HC content will begin to rise. As ϕ increases above one, HC and CO emissions rise as excess HC and CO is exhausted due to incomplete combustion, while NO emissions fall due to lower temperatures.

During the compression phase in the two-stroke cycle, oil layers along the cylinder walls absorb HC while an unburned air-fuel mixture is pushed in between the piston and cylinder walls. In the combustion phase, NO forms from chemical reactions between nitrogen and oxygen molecules in burned gases at high temperatures, with higher temperatures leading to higher NO formation rates. Excess NO is exhausted during the expansion stroke. CO pollutants also form in high temperatures in the combustion phase and freeze after NO emissions in the expansion phase, with HC outflowing from the crevices during the downstroke [8]. In fuel rich mixtures, CO is left over due to insufficient oxygen molecules to combust with the fuel, reducing CO_2 levels. In leaner fuel mixtures, dissociation of CO_2 leads to significant levels of CO [12]. In the exhaust phase of the two-stroke cycle, HC build-up on the cylinder walls is scraped off by the piston, HC in the oil layers is desorbed, and HC is entrained from the cylinder wall [8].

Pollutant formation during the compression, combustion, expansion, and exhaust phases is illustrated in Figure 6. Note that Figure 6 illustrates the four-stroke cycle. In the two-stroke cycle, the exhaust ports are located on the cylinder liner and the piston does not scrape over the portion of the cylinder that is exposed to combustion gases, so the behavior of HC species differ.

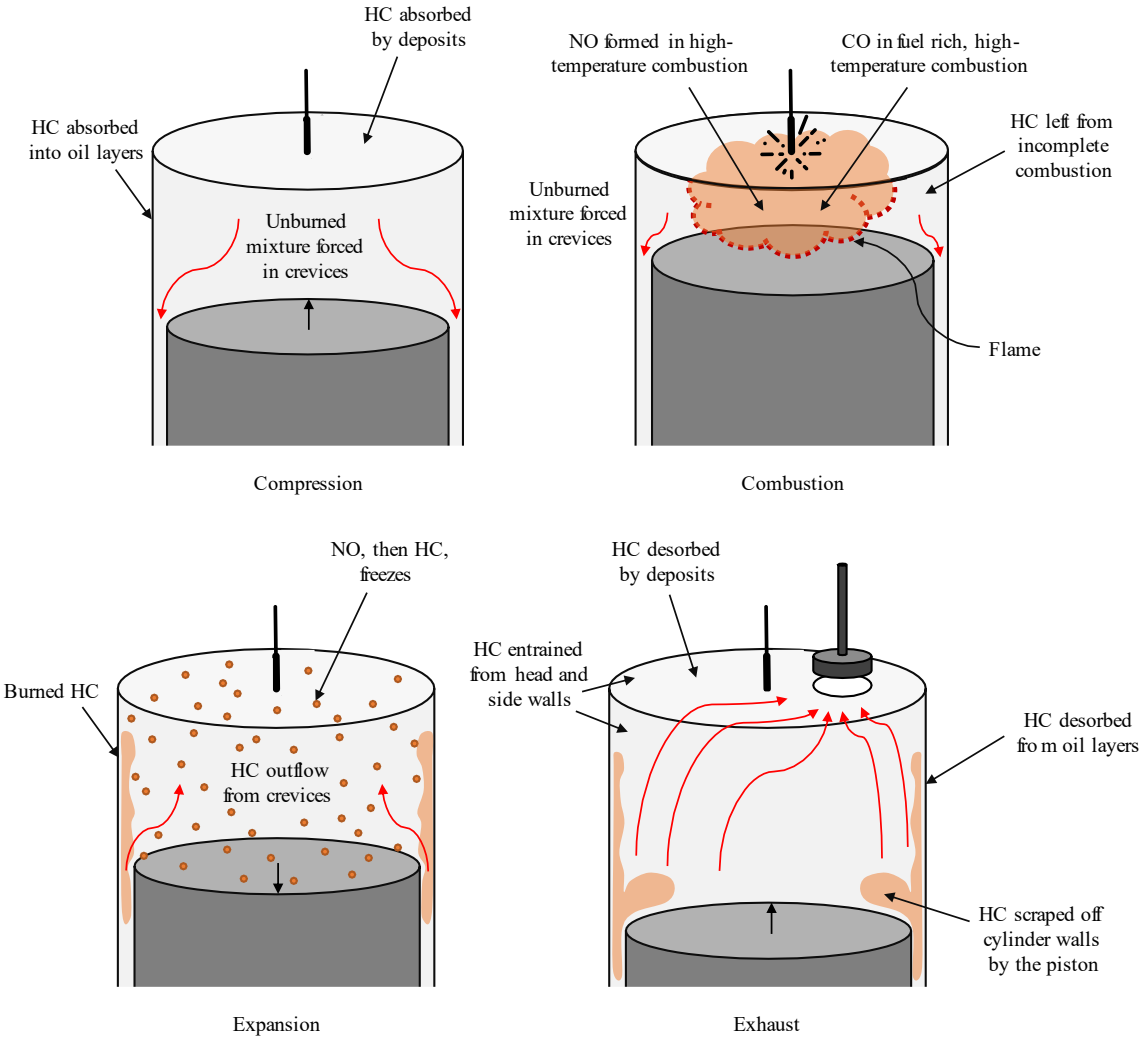

Figure 6: Formation of NO, HC, and CO during compression, combustion, expansion, and exhaust phases of a two-stroke engine cycle. Adapted from [8].

2.1.1. Oxides of Nitrogen (NO_x)

In near-stoichiometric fuel-air mixtures, the extended Zeldovich mechanism, characterized by reactions (1) and (2), is widely accepted as the primary source of nitric oxide formation inside the engine's cylinder [13]. Lavoie et al. added reaction (3) for its contribution to NO formation due to reactions between nitrogen and hydroxide [14].

$$O + N_2 \leftrightharpoons NO + N \quad (1)$$

$$N + O_2 \leftrightharpoons NO + O \quad (2)$$

$$N + OH \leftrightharpoons NO + H \quad (3)$$

Through reactions (1) to (3), NO is formed in the flame front and in post-flame gases. NO developed by post-flame gases tends to dominate NO formed by the flame front because the flame reaction zone is thin and does not last long, and temperatures produced after combustion tend to be higher due to cylinder compression [8]. NO_2 is formed in the flame zone via reactions between NO and hydroperoxyl (HO_2), shown in reaction (4) [15]. The reverse reaction to convert NO_2 into NO is shown in reaction (5). Note that the reaction between NO_2 and O to form NO and O_2 will not occur if NO_2 is quenched [16].

$$NO + HO_2 \rightarrow NO_2 + OH \quad (4)$$

$$NO_2 + O \rightarrow NO + O_2 \quad (5)$$

Figure 7 shows NO and NO_2 production in a spark-ignited engine. The ratio between NO_2 and NO reaches its maximum just below its stoichiometric point at an equivalence ratio of 0.85, when the fuel-air mixture is lean. Total oxides of nitrogen are the summation of NO and NO_2 formed throughout the combustion process [8].

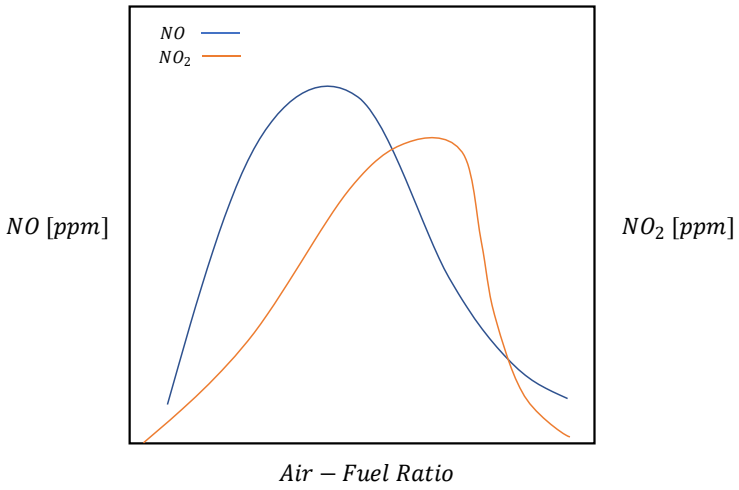

Figure 7: NO and NO_2 production in a spark-ignited engine with respect to increasing air-fuel ratio. Adapted from [8].

2.1.2. Unburned Hydrocarbons (HC)

HC pollutants exit the exhaust in two peaks: the first peak is caused by HC entrainment on the head wall quench layer during the first blowdown when the exhaust port opens before the piston reaches bottom dead center (BDC); the second HC peak occurs during HC entrainment of the side wall vortex during the exhaust stroke, commented on Figure 8 [17]. The first peak may be a result of a rich fuel-air mixture, with hydrocarbons building up along the cylinder walls without combusting.

Alternatively, if the fuel-air mixture is too lean, HCs can rise due to incomplete combustion or engine misfires.

HCs are formed via four mechanisms: filling crevices with unburned HCs, oil layers on the intake walls, incomplete combustion, and flame quenching on the combustion chamber walls [8] [18]. Through the four formation mechanisms, hydrocarbons are able to avoid complete combustion without oxidizing, releasing into the atmosphere as unburned hydrocarbons [8]. Small aromatic HCs can also be formed in the flames of a rich fuel-air mixture [19] [20].

Most of the HC emissions are a product of filling crevices with unburned HCs, with oil layers and deposits being the next highest source of HC emissions, and flame accounting for the rest of HC emissions. When the engine is started and not yet warmed up, HC emissions are higher due to lower temperatures in the crevices and oil layers [18].

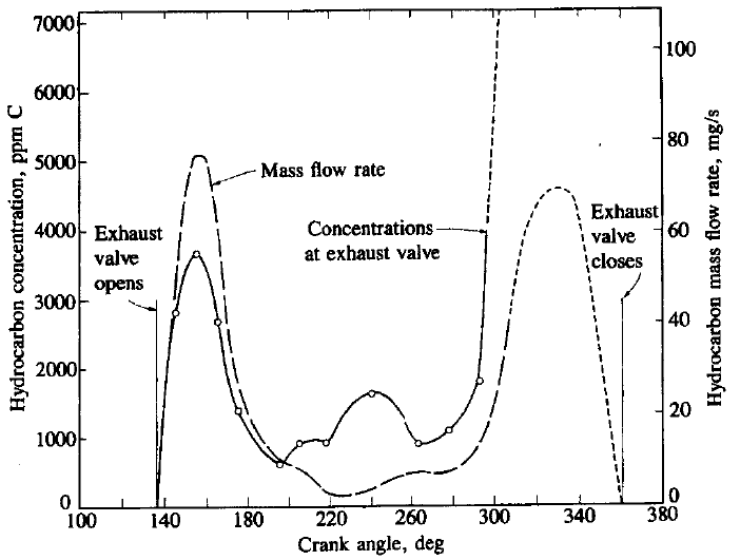

Figure 8: HC concentration and mass flow rate at the exhaust of a spark-ignition engine. Reprinted from [8].

2.1.3. Carbon Monoxide (CO)

In spark-ignited (SI) engines, CO emissions are directly influenced by air-fuel ratio. As the fuel-air mixture becomes increasingly rich in a spark-ignited engine, CO increases linearly at the exhaust, whereas CO emissions remain low in leaner fuel-air mixtures (Figure 9). In a conventional spark-ignited engine, the fuel-air mixture is close to stoichiometric under partial loadings, then increases in richness with increasing load. As a result, CO emissions tend to increase in SI engines as load increases. To combat higher CO emissions, supplying the engine with a leaner fuel-air mixture will decrease CO concentrations [8].

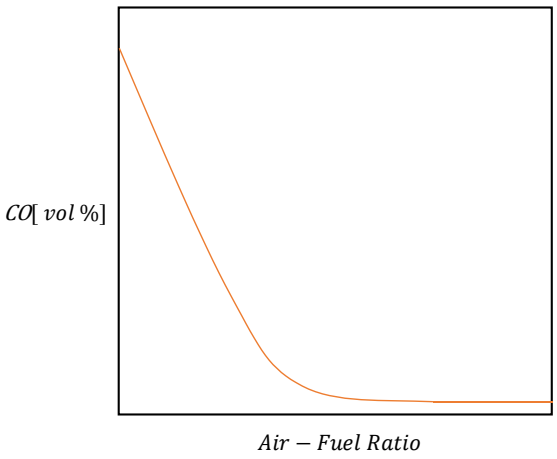

Figure 9: CO concentration in a spark-ignited engine with respect to increasing air-fuel ratio. Adapted from [8].

2.1.4. Methods to Reduce Harmful Emissions in SI Natural Gas Engines

Natural gas engines tend to produce lower emissions than gasoline-fueled engines [21], as natural gas engines have lower CO_2 concentrations due to stoichiometry.

Typically, CO emissions are lower in natural gas engines than gasoline engines by approximately 50% to 90% (except at lower equivalence ratios) [22], and unburned HCs are lower by 55% [23]. In some cases, unburned HCs are higher in natural gas engines than in gasoline engines, but this depends on the design and setup of each engine. NO_x in SI natural gas engines can be reduced through the introduction of exhaust gas catalysts [22]; however, catalysts that can be used under lean fuel-air mixtures in natural gas engines are expensive. As an alternative to reduce NO_x emissions, a diluent, such as exhaust gas recirculation (EGR), can be introduced to reduce oxygen concentration, increase specific heat capacity in the natural gas-air charge, and reduce flame speeds. NO_x concentration decreases with the introduction of a diluent because peak combustion temperatures are decreased. As the concentration of diluent, such as EGR, increases, NO_x levels continue to decrease [22]. EGR can reduce HC emissions up to a point, then HC levels begin to rise with increasing EGR.

Introducing hydrogen gas into natural gas fuel will decrease unburned HC and CO emissions, but increase NO_x emissions by speeding up combustion due to a higher flame velocity [22] [24]. The increase in NO_x emissions is a result of higher combustion temperatures, which Korakianitis et al. were able to combat in an SI engine by increasing EGR using a 10% hydrogen and 90% natural gas-fuel ratio. When blending other fuels with natural gas, combustion and performance is improved as long as the fuel being blended into the natural gas produces a higher laminar-flame speed [25].

Additionally, using a direct fuel injection system, rather than port fuel injection, increases the engine's operating pressures and allows for leaner air-fuel mixtures for the

engine [22]. As a result, NO_x emissions are reduced due to charge stratification [26]. Modifying fuel-injection timing also plays a role in reducing emissions. With advanced injection timing, NO_x concentrations increase significantly as injection occurs earlier during the compression stroke but remain relatively constant when further advanced into the intake stroke. Unburned HCs, however, decrease with advanced spark timing, and CO emissions do not change considerably [27]. Other studies indicate that both HC and CO emissions in compressed natural gas (CNG) engines increase considerably when spark timing is retarded [28] [29] [30].

Precombustion chamber (PCC) technology is used as another injection method to reduce NO_x, HC, and CO emissions from natural gas engines. PCCs are discussed in more detail in the following sections.

2.2. Precombustion Chambers (PCC)

A PCC can be introduced to a natural gas engine setup to combat harmful emissions. A PCC is a small chamber, about 1% to 2% of the main chamber's clearance volume, which ignites a near-stoichiometric to slightly rich air-fuel mixture and ejects combustion radicals into the main chamber (Figure 10). As a result of increased pressure inside the PCC, approximately one million times greater ignition energy is released into the main chamber compared to a normal spark plug [2] [3] [4]. Combustion stabilizes at lean operating conditions in the main chamber and in-cylinder temperatures are reduced, which reduces CO, HC, and NO_x emissions.

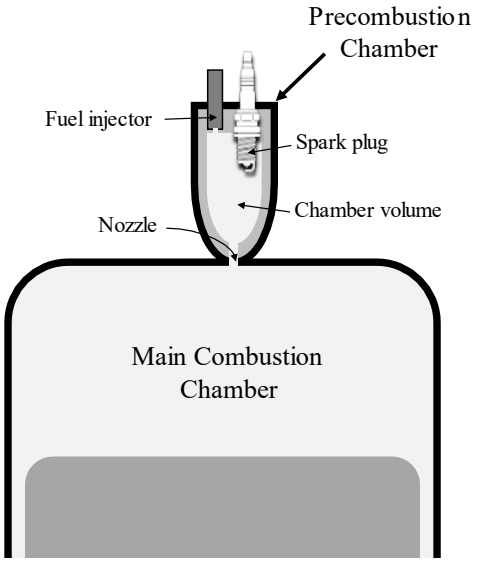

Figure 10: SI engine with a precombustion chamber.

2.2.1. Prechamber Contribution to Emissions

In open chamber (OC) engine operation (i.e. a spark plug connected to the main combustion chamber (MCC) rather than a PCC connected to the MCC), NO_x emissions can be reduced by using a lean air-fuel ratio. However, operating with an OC setup at a very lean condition causes spark misfiring and unstable combustion, resulting in significantly increased CO and HC emissions. Operating a two-stroke SI engine with a PCC allows for stable combustion and reduced cycle-to-cycle combustion variation. Stable combustion occurs because the ignition volume in the MCC is large, and thus, ignition is not as affected by mixture heterogeneity. Additionally, PCCs allow for the MCC to operate with much leaner air-fuel mixtures because the energy released by the PCC is high and spatially distributed [2]. As a result, NO_x emissions can be reduced significantly, compared to OC operation, due to lower in-cylinder temperatures and less

variation across engine cycles [31]. Combustion duration is also reduced due to shorter distances for the MCC flame front to travel [3].

Gingrich et al. found that a prechamber contributed to only 10% of NO_x emissions in a Waukesha four-stroke natural gas engine at nominal engine conditions, but when the engine operated with a lean mixture at medium speed, the PCC contributed to 85% of engine-out NO_x emissions [32]. Olsen and Lisowski found that PCCs do contribute to the majority of engine-out NO_x emissions in a Cooper-Bessemer natural gas engine, though the NO_x within the PCC was lower than at the exhaust, since the MCC no longer generates high NO_x emissions. Thus, the researchers concluded that NO_x formed by a PCC occurs just outside the PCC in the jet ejected into MCC. Olsen and Lisowski further explored a PCC's effect on NO_x emissions by testing a dual PCC setup on the Cooper-Bessemer engine. The researchers determined that with dual PCCs, NO_x emissions were measured to be 42% higher [2]. With a single PCC installed, NO_x emissions were lower than OC operation.

Moreover, CO and HC emissions were measured to be high in all cases with dual PCCs compared to single PCC operation [2]. In some cases, PCCs also increase overall CO, HC, and NO_x emissions due to their stoichiometric or rich operation while the engine is operating at nominal conditions [33]. Olsen and Lisowski also found that CO can be significantly reduced while using one PCC and operating the engine with high boost. Though the MCC operates with a lean mixture, which reduces engine-out CO emissions, the PCC releases CO at one to two times higher levels than from the exhaust port, contributing to the majority of the engine's CO emissions. Within the PCC, CO is formed

and then oxidized in the main chamber; however, significant amounts of CO emissions do not get oxidized and are released into the exhaust [2].

NO_x formation from a PCC starts with a stoichiometric reactant mixture within the PCC and a lean mixture within the MCC. Figure 11 shows the mixtures in both the PCC and MCC before ignition occurs. The air-fuel mixture in the PCC may be richer than stoichiometric in some cases.

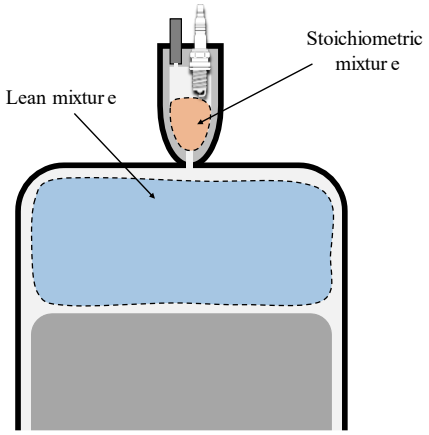

Figure 11: PCC and MCC configuration before ignition. Adapted from [2].

After ignition occurs, the explosive jet from the PCC fires into the MCC (Figure 12). The explosive jet consists of reactants, hot combustion products, and burning gases as combustion occurs [4]. Olsen and Lisowski determined in their study that combustion in the PCC is incomplete; thus, the jet firing into the MCC is considered to be only partially combusted. As the jet continues to flow into the MCC, the jet burns continuously and hits the piston bowl [34].

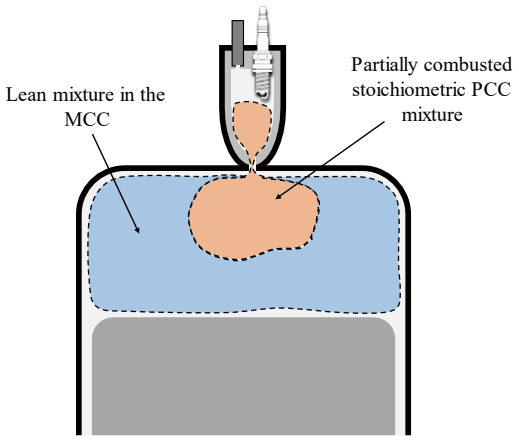

Figure 12: Partially combusted jet from PCC into MCC. Adapted from [2].

Once the air-fuel mixture is fully combusted within the MCC, a stratified mixture remains in the MCC. Combustion products come from the stoichiometric mixture region, caused by the PCC's jet, and from a surrounding lean mixture. The stoichiometric region is characterized by a high temperature and high NO_x emissions, while the lean mixture is characterized by a low temperature and low NO_x emissions (Figure 13). Pressure rises in the MCC, then the flow from the MCC reverses and the gases go back into the PCC with an unknown composition. The gases flow back out of the PCC during expansion and exit the exhaust through the MCC. During combustion, NO_x increases as gases flow back into the PCC until peak pressure is reached (temperature also increases with an increase in pressure, supporting NO_x development), then NO_x decreases as pressure declines during the expansion stroke (temperature decreases as well) [4].

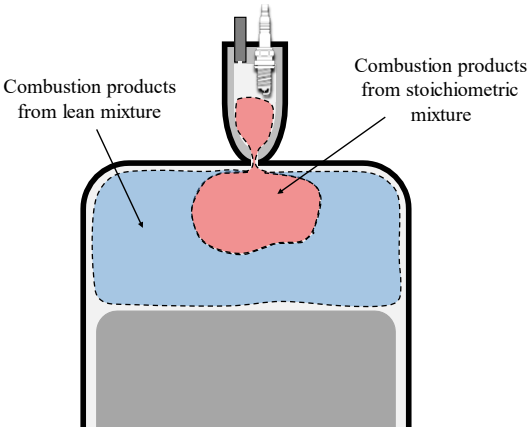

Figure 13: Combustion products resulting in a stratified mixture in the MCC. Adapted from [2].

2.2.2. Prechamber Design

PCC design can vary greatly, providing dramatic improvements in performance with small design changes. The PCC's volume, nozzle size, and length-to-diameter ratio all contribute to PCC performance. In terms of volume, a PCC is approximately 1% to 2% the volume of the MCC, depending on the NO_x reduction to efficiency ratio [4]. As PCC volume increases, brake specific fuel consumption (BSFC) decreases, NO_x emissions increase, and CO emissions increase. Reinbold determined that an optimal trade-off occurs between NO_x emissions and efficiency at a PCC volume of 2% [10].

When the PCC operates with a slightly rich mixture with an equivalence ratio between 1.1 and 1.2, the main chamber can operate at leaner fuel conditions with an equivalence ratio of around 0.4 [35]. An optimal PCC length-to-diameter ratio for optimal fuel-air mixing within a prechamber is 1.5 [36]. With an optimized PCC length to diameter ratio, recirculation reaches the full length of the PCC [4], and the range of fuel-air ratio increases [35]. The spark plug should be configured close to the PCC's nozzle,

as this configuration increases pressure rise and allows for the fuel-air mixture to burn more effectively. The farther away the spark plug is from the nozzle, the more unburned fuel and raw air is forced into the MCC [4].

2.2.2.1. Nozzle Configuration

The optimal nozzle design is given by β, a dimensionless throat area, and the Craya-Curtet number, C_t. β is given by equation (6), where *B* is the engine bore, A_t is the throat area, and V_p is the prechamber volume. In a study by Watson et al., the optimal β was determined to be 0.41 to optimize PCC efficiency to NO_x emissions [37].

$$\beta = B * \frac{A_t}{V_p} \tag{6}$$

C_t is given by equation (7), where *D* is the inside diameter of the PCC and *d* is the nozzle's diameter. In a study by Anderson et al., the optimal C_t was determined to be 0.3 to optimize PCC efficiency and NO_x emissions [35]. Both C_t and β influence the PCC's jet speed and displaced mass [4]. When C_t reaches 0.3 or greater, mixing within the PCC is not sufficient enough for stable combustion, while a C_t of less than 0.2 results in poor ignition. Olsen et al. determined that for stable combustion, a C_t of 0.22 to 0.3 is sufficient for mixing within the PCC, with a PCC length-to-diameter ratio of 2 allowing for sufficient mixing as well [4].

$$C_t = \left[\left(\frac{D}{d}\right)^2 - \frac{1}{2}\right]^{-\frac{1}{2}} \quad (7)$$

In a study by Olsen et al., the nozzle was modified to have an angle of 20-degrees from the PCC's centerline, rather than 0-degrees. Initially, with a nozzle design along the PCC's centerline, the jet blasting from the PCC into the MCC spreads evenly across the piston's surface. Though effective at transferring heat, the nozzle along the PCC's centerline caused the piston to cool and quench the jet's combustion, reducing the jet's effectiveness at fully combusting the MCC's lean mixture. Thus, a 20 degree angle from the centerline in the nozzle prevents piston cooling and quenching combustion in the jet (Figure 14) [4].

Figure 14: Nozzle with 20 degree angle from PCC centerline (line) and nozzle along PCC centerline (right). Reprinted from [4].

By changing the nozzle's angle from 0-degrees to 20-degrees along the PCC centerline, Olsen et al. found a 27.6% decrease in standard deviation of peak pressure, 2.27% decrease in BSFC, 19.9% decrease in brake specific NO_x ($BSNO_x$), 0.56% decrease in brake specific CO (BSCO), 11.5% decrease in brake specific THC (BSTHC), and 3.83% decrease in brake specific CH_2O ($BSCH_2O$) [4]. Simpson and Olsen tested a baseline PCC, nonfueled micro PCC (NF MPCC), a multiple nozzle PCC, an adiabatic PCC, a fueled micro PCC (fueled MPCC), a standard Cooper PCC with an electronic check valve (ePCC), and a nonfueled micro PCC with high pressure fuel injection (NF MPCC HPFI). The multiple nozzle PCC featured three nozzles angled to fire the jet parallel to the piston surface. The MPCC variations also had a modified nozzle with three smaller nozzles [3]. Note that the nozzle summed areas of the smaller nozzles were equal to the area of a single, standard nozzle size. All of the concept PCC designs improved the results of the baseline PCC, with the fueled MPCC providing the largest decrease in NO_x emissions of more than 50%, with a decrease in CO and THC of 40% in each. CO was reduced slightly with the multiple nozzles and fueled MPCC configurations due to ignition improvements from a richer mixture outside of the PCC volume and overall volume reduction [3]. Simpson and Olsen found that PCC volume reduction contributed most to minimizing the NO_x and CO tradeoff.

2.2.2.2. Orifice Size and Check Valve

The PCC's check valve, which contains an orifice that can vary in size, meters fuel flow, allowing for fuel to flow into the PCC during the scavenging process while

preventing fuel from flowing into the PCC during compression, combustion, and expansion [2]. Olsen et al. found that using a slightly larger orifice of 0.039", rather than 0.031", helped compensate for combustion variability [4]. Larger orifice sizes result in higher PCC pressure rises. In a study performed by Cooper Machinery Services on an Ajax E-42 natural gas engine, the researchers determined that of the 0.023", 0.029", and 0.038" orifices, the smallest orifice size provided the best results in their mechanical check valve. The other orifices resulted in poor combustion, allowing the engine to fire two or three times before it would stop firing altogether. The inlet pressure into the main chamber was approximately 42 psi and the inlet pressure into the PCC was approximately 13 psig [38]. Note that with Cooper's PCC and orifice of 0.023", NO_x concentration increased compared to OC operation.

Simpson and Olsen determined that using an electronic check valve in their PCC (ePCC), CO was reduced slightly, and THC was reduced heavily at partial load due to improved mixing attributed to the electronic check valve. At full load, NO_x reduction was dominant in the ePCC, with an approximate 43% reduction [3]. In a study by Olsen et al., when using an electronic check valve with a nozzle design at 20-degrees, NO_x, BSFC, and CH_2O were reduced by 20%, 4%, and 4%, respectively [4].

2.3. Flame Kernel Development

In a spark ignited engine, an ionized plasma channel is created through discharge at a given spark timing, which unloads ignition energy to the fuel-air mixture (Figure 15) [8]. After ignition energy is unloaded, flame initiation (i.e. flame kernel) is formed along

the high temperature plasma channel. In order for steady combustion to occur, the ignition energy must be greater than the minimum ignition energy required during the initial flame kernel decay at peak temperature [39]. In a lean burning engine setup, such as a PCC configured two-stroke engine, early flame kernel initiation is important for combustion, requiring high ignition energy and multiple initial flame kernels. Zhu et al. determined that with sufficient discharge energy, flame growth rates are faster due to a larger initial flame kernel, benefiting combustion [40].

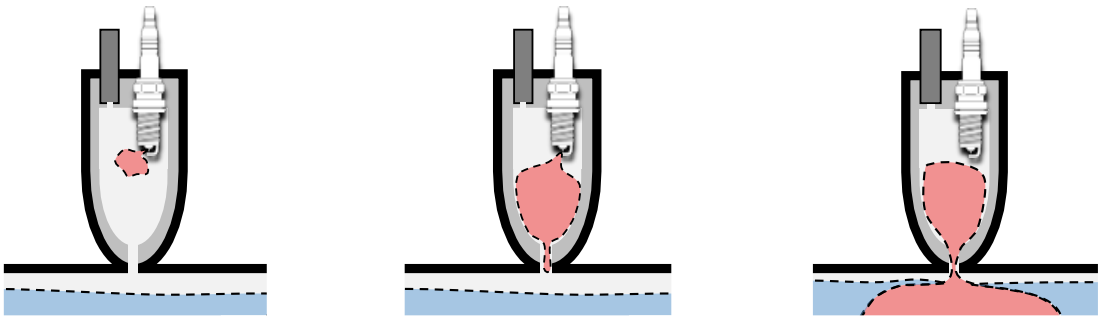

Figure 15: PCC flame kernel development and flame propagation into the MCC.

Prechambers provide high ignition energy, resulting in multiple ignition sites with fast burn rates. The partially combusted products from the PCC ejected into the MCC initiates combustion in the main chamber, allowing for much leaner mixtures within the MCC compared to an OC configuration [41]. Attard and Parsons used a PCC on a single cylinder engine and determined that a PCC can tolerate up to 54% mass fraction diluent, which increased fuel economy by 18% and reduced NO_x to close to zero. Flame kernel development with a PCC was mostly unaffected by changes in spark plug rotation and

depth, electrode gap, and spark plug type due to the PCC's robust design. The jet expelling from the PCC ignites the MCC mixture with a distributed ignition source, which does not need to rely on a single flame kernel to initiate combustion within the MCC. Thus, changes in the spark plug do not significantly affect flame kernel development using a PCC. However, providing a flush-mounted spark plug on the PCC allowed for a 2% improvement to dilution level by reducing trapped residuals [41]. In an OC configured engine, spark plug variations greatly change flame kernel development and can affect combustion stability.

Overall, a lean mixture inside of the MCC requires early flame kernel initiation and high discharge energy to combust the mixture. A PCC provides extremely high discharge energy, expelling a partially combusted mixture that allows the MCC mixture to combust. Changes in the spark plug are not needed when using a PCC as long as the PCC is able to combust, though a flush spark will slightly improve the dilution level.

3. EXPERIMENTAL METHODS

3.1. Equipment

3.1.1. Ajax E-565 Natural Gas Engine

The engine used during this study was a single cylinder, two-stroke Ajax E-565 natural gas engine, with specifications listed in Table 1. Fuel is injected using a direct injection system and then ignited using an Altronic NGI-1000 ignition system.

Table 1: Ajax E-565 natural gas engine specifications. Adapted from [42] [43].

Parameter	Value
Rated Continuous Power	40 hp
Torque	400 ft-lb
Rated RPM	525 RPM
Recommended Speed Range	300 – 525 RPM
Bore x Stroke	8-1/2 in x 10 in
Displacement	9.29 L
Compression Ratio	6:1
Engine Weight	4420 lbs
Flywheel Weight	1500 lbs

Figure 16 shows the new PCC fuel line installed on the Ajax E-565 in AERL's lab, shown in the lower left-hand corner of the figure. Natural gas composition of the fuel entering the engine's main chamber and prechamber can be found in Appendix A. The PCC fuel line is discussed in further detail in the next section.

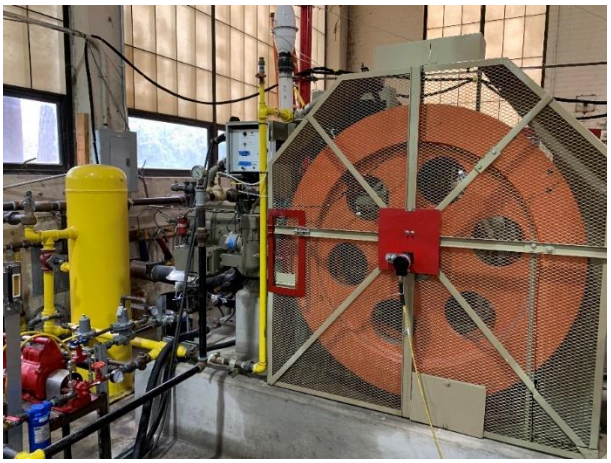

Figure 16: Ajax E-565 engine with PCC fuel line installed.

3.1.2. Prechambers and Prechamber Fuel Line

3.1.2.1. Prechambers Provided by Cooper Machinery Services

Cooper Machinery Services provided three prechambers for this study: a standard SIP for bore sizes of 10.5 inches up to 13.25 inches, a #10-GMVH-13-10 Eco-Jet prechamber, and a GMVH-13-11 Eco-Jet prechamber (Figure 17). The first SIP (P1) has a diameter of 2.3 inches at the spark plug port, a diameter of 1.65 inches just upstream of the nozzle, and a total length of 2.45 inches, with an approximate volume of 7.6 cubic inches. P1 fit a Champion W18 spark plug, which is the same spark plug used for OC engine operation. The #10-GMVH-13-10 Eco-Jet prechamber (P2) has a diameter of 1.9 inches and an approximate length of 2.6 inches (accounting for spark plug thread depth), with an approximate volume of 7.4 cubic inches. Lastly, the GMVH-13-11 Eco-Jet prechamber (P3) has a diameter of 1.6 inches and an approximate length of 2.2 inches (accounting for spark plug thread depth), with an approximate volume of 4.4 cubic inches. Both P2 and P3 fit an NGK Iridium WR5IX spark plug.

Figure 17: P1 (top), P2 (middle), and P3 (bottom).

P1 and P2 both have nozzle outlets that follow the prechamber's center axis line (0 degrees from the center axis line) and P3 has a nozzle outlet that has a center point located 0.9 in away from the center axis line (Figure 18). P1 has a nozzle with a diameter of 0.25 in, while P2 and P3 each have a slightly larger diameter of 0.26 in.

Figure 18: PCC nozzles with P1 (left), P2 (middle), and P3 (right).

Each prechamber also has an inlet and outlet port for a water line to keep each prechamber cooled. An Oase Aquarius Universal 370 water pump with a 370 gph max flow rate was used in a 5-gallon bucket of cold water to keep the prechambers cool during

operation. P2 and P3 used an NGK Iridium WR5IX spark plug, which is much smaller than the Champion W18 spark plug used for P1. Cooper Machinery Services tested the P1 in their facility and experienced unstable combustion. With an orifice of 0.023" in the PCC's check valve (check valve opens when 3.5 to 4 psi is applied), an inlet pressure of 13 psig upstream of the PCC, and an inlet pressure of 42 psi upstream of the main chamber, Cooper Machinery Services was able to get the Ajax E-42 engine to fire with fewer misfires, though still not with optimal combustion [38]. P2 and P3 prechambers were not previously tested by Cooper Machinery Services on an Ajax E-565 engine. Table 2 summarizes the prechamber specifications.

Table 2: PCC specifications.

Parameter	P1	P2	P3
Diameter	2.3 in / 1.65 in	1.9 in	1.6 in
Length	2.45 in	2.6 in	2.2 in
Volume	7.6 in^3	7.4 in^3	4.4 in^3
L/D Ratio	1.07 / 1.48	1.37	1.38
C_t	0.122 / 0.180	0.147	0.178
Orifice	0.019 in	0.019 in	0.019 in
Spark Plug	Champion W18	NGK Iridium WR5IX	NGK Iridium WR5IX
Nozzle Diameter	0.25 in	0.26 in	0.26 in
Water Pump	Oase Aquarius Universal 370	Oase Aquarius Universal 370	Oase Aquarius Universal 370
Max Water Pump Flow Rate	370 gph	370 gph	370 gph

Due to Cooper Machinery's success using their smallest 0.023" orifice in P1's check valve, an orifice size of 0.019" was used for each check valve in P1, P2, and P3 in this study, as it was the smallest orifice available. The Ajax E-565 successfully fired for all PCCs while using the 0.019" orifice, as the 0.019" orifice provided the largest range for adjusting pressure and fuel flow. Figure 19 shows an exploded view of the check valve used for P1, P2, and P3.

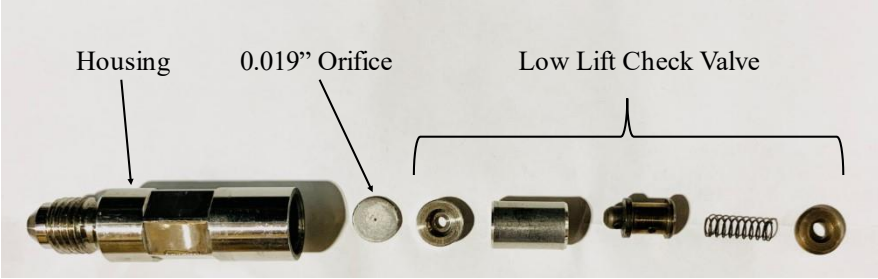

Figure 19: PCC check valve with 0.019" orifice.

3.1.2.2. Prechamber Fuel Line

Cooper Machinery Services provided a Parker 401219 fuel filter, a Reliance UA300 AC motor and pump (not used in this study), a Fisher Type 119 fuel gas regulator, and a Fisher Type 67C valve. Additional ¾-inch NPT tees, ¾-inch NPT ball valves, a ¾-inch NPT high-pressure adjuster valve, a ¾-inch NPT check valve, reducing adapters, a ¼-inch NPT PCC fuel hose, and a fuel flow meter were installed to complete the PCC fuel line configuration. Figure 20 is a schematic of the PCC plumbing and Table 3 is a summary of the parts installed.

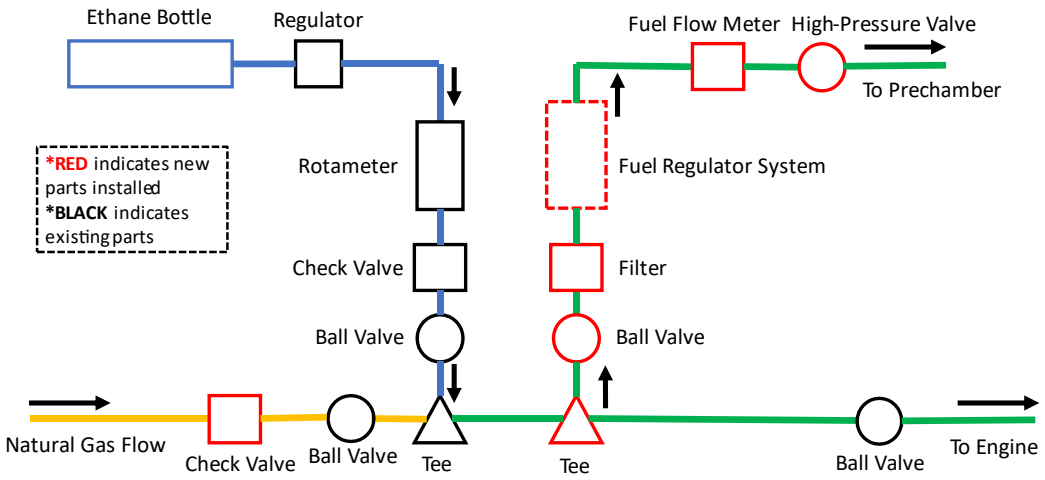

Figure 20: New PCC fuel line plumbing for the Ajax E-565 natural gas engine.

Table 3: Parts installed for PCC fuel line plumbing.

Item Description	Make / Model #
Filter	Parker 401219
AC Motor / Pump	Reliance UA300
Fuel Regulators	Fisher Type 119 and 67C
¾" NPT Check Valve	In-house
¾" NPT Tee	4429K254 (McMaster)
¾" NPT Ball Valve (2)	4726K49 (McMaster)
¾" NPT High-Pressure Adjuster Valve	4737K54 (McMaster)
Fuel Flow Meter	Alicat
Straight Connectors (2)	50785K95 (McMaster)
Reducing Adapters (2)	Lowes
Stainless Steel Fuel Hose	5793T62 (McMaster)
¾" NPT Steel Pipe	In-house
Pressure Gauge (2)	In-house
Additional Parts as Needed by SSC	In-house

The Type 119 fuel regulator and Type 67C valve function by first releasing the Type 67C valve via spring actuation with 0 psi to 35 psi loading pressure (5 psi to 35 psi recommended). Spring actuation occurs by applying the loading pressure to the gas valve diaphragm, which moves a disk holder away from the orifice. As loading pressure decreases, the spring force closes the disk holder, which results in a spring-close action if the loading supply pressure suddenly decreases [44]. Natural gas then enters the inlet of the Type 67C valve and is released through the outlet, which then enters the loading pressure port of the Type 119 fuel regulator, which releases fuel flow via the same actuation method as the Type 67C valve (but with a range of 5 psi to 35 psi). Next, fuel flowing into the Type 119 regulator is then released through the outlet, the fuel flow meter, the high-pressure valve, the fuel line, and into the PCC. Figure 21 shows the schematic for the fuel regulator system. The fuel regulator system serves as an extra layer of safety. Both the Type 119 and Type 67C regulator valves fail when closed; if pressure loss occurred on the main fuel line, the regulator valves would close and prevent backflow into the fuel line.

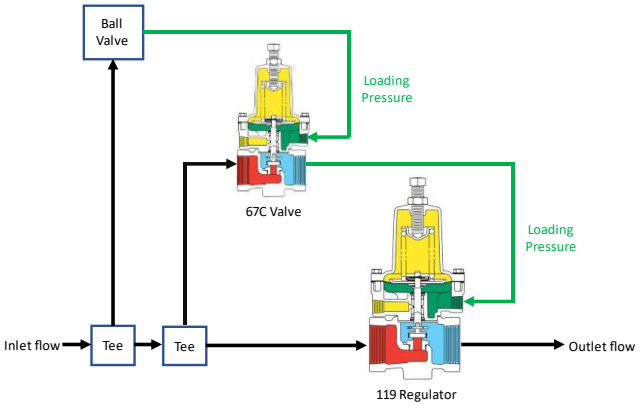

Figure 21: PCC fuel regulator system for the Ajax E-565 natural gas engine.

Figure 22 shows the final PCC fuel line system installed. Note that the plumbing was designed to incorporate the existing ethane fuel line for use in future ethane blending experiments while operating the engine with a prechamber. The AC motor and pump was bypassed and not used during this study.

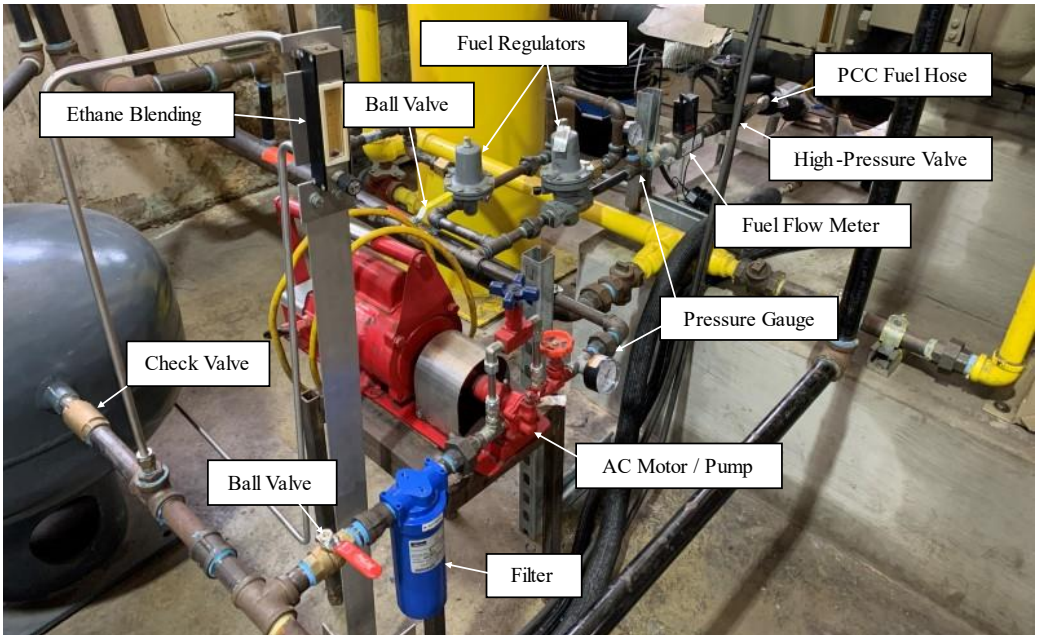

Figure 22: PCC fuel line.

3.1.3. Altronic NGI-1000 Ignition System

The ignition system installed on the Ajax E-565 engine is the Altronic NGI-1000, a solid-state digital ignition system, which replaced the original Altronic I ignition system. The Altronic NGI-1000 uses an angular pickup input signal from a magnetic pickup sensor, receiving timing inputs directly from the engine's crankshaft, and allows for advanced spark energy control. Altering spark energy allows for enhanced combustion during lean-burn operation [45].

3.1.4. Taylor DEA150 Dynamometer

The Taylor DEA150 dynamometer is an air-cooled eddy current engine dynamometer with a limit of 150 hp and 3500 rpm shaft speed (Figure 23). The Taylor DEA150 weighs 1300 lb and has a heat load of 115 kW per hour from the dyno [46]. A dynamometer, such as the Taylor DEA150, applies a braking torque and measures the resulting force acting on a lever arm in order to calculate torque and power from the measurements.

Figure 23: Taylor DEA150 dynamometer.

3.1.5. Data Acquisition System

The Data Acquisition (DAQ) system is a National Instruments (NI) cDAQ with NI components that collect in-cylinder, intake, and exhaust data from pressure transducers, thermocouples, and fuel flow meter (Figure 24). Data is collected every quarter crank angle degree, up to 360 degrees, and is compiled using a Matlab script written by AERL. The compiled data is then post-processed and used to calculate engine performance parameters and efficiencies.

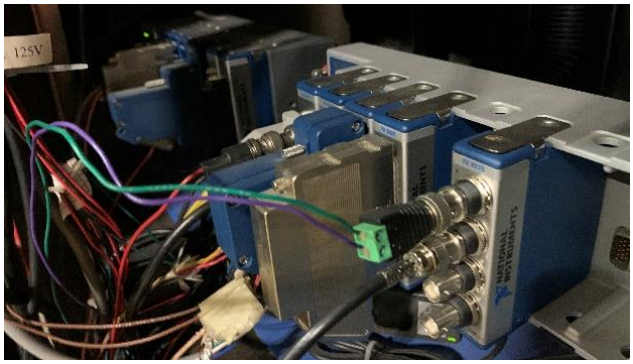

Figure 24: cDAQ with NI components.

3.1.6. Horiba MEXA-7100D Emissions Bench

Emissions measurements are collected through the Horiba MEXA-7100D emissions bench, which measures CO, CO_2, O_2, THC, and NO_x emissions (Figure 25). Gas measurements are performed through the main control unit (MCU) [47], and CO / CO_2, O_2, THC, and NO_x emissions are measured via AIA-72X, MPA-720, FIA-725A, and CLA-720MA analyzers, respectively.

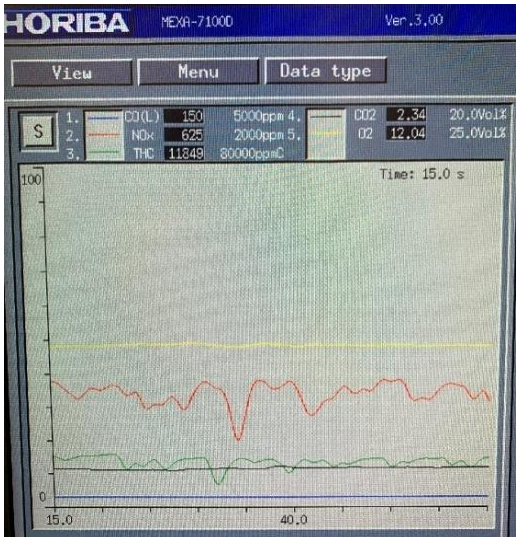

Figure 25: Horiba MEXA-7100D emissions measurement during PCC operation.

CO and CO_2 are measured with the AIA-72X analyzer at the engine's exhaust using non-dispersive infrared absorption (NDIR). NDIR determines concentration by measuring absorption of infrared energy in atoms at constant pressure and different wavelengths [48]. O_2 is measured with the MPA-720 analyzer, which uses magneto-pneumatic detection (MPD). MPD uses oxygen's sensitivity to magnetic fields to measure concentration by sending oxygen molecules through a magnetic field. Pressure changes around the magnetic poles when oxygen flows through the field, which provides oxygen's concentration as it changes with pressure. NO might interfere slightly with O_2 measurements, but within ± 0.05 vol% O_2 [49]. THC is measured in the Horiba emissions bench with an FIA-725A analyzer, which uses flame ionization detection (FID) to measure ions generated by heat energy, which is proportional to the carbon atoms in the exhaust [50]. Lastly, NO and NO_x concentrations are measured with the CLA-720MA analyzer, which uses chemiluminescence (CLD) to measure the released light energy when NO_2 returns to a ground state after being transformed from an NO and O_3 reaction [51].

3.2. Procedure

3.2.1. Open Chamber Testing

Operating the Ajax engine is accomplished using AERL's Ajax start-up and shut-down procedure. The main gas valve and three other valves were turned to the open position on the natural gas line. Next, the starter was plugged into the side of the ignition box to crank the flywheel and provide energy to the ignition starter. The DAQ, emissions bench, Matlab software, and ignition software were then turned on and given

approximately 15 to 30 minutes to warm up. When turning on the emissions bench, the appropriate gas chambers were opened first (shown in Figure 26). A voltmeter was connected to measure load applied to the engine by the dynamometer, which is itself manually controlled by a potentiometer. Changes in load cell voltage were previously calibrated against measured changes in dynamometer torque.

Figure 26: Gas chambers for Horiba emissions bench.

When starting the engine, the "Push to Start" button was held to crank the flywheel while simultaneously throttling the fuel valve after the flywheel reached its peak speed. Once the engine began firing with successful combustion, the engine's speed was brought up to 500 RPM, then allowed to warm up for 5 to 15 minutes before collecting data. Once data was ready to be collected, the amplifier for the in-cylinder pressure transducer was turned on and set to "Operate."

For this study, two speeds and loads were used to collect and analyze data: low speed and low load, and high speed and high load. In this study, low speed was classified as 430 RPM, low load was 62.5% of full load (corresponding to a load cell voltage of

0.0025 V), high speed was classified as 500 RPM, and high load was 100% load (or a load cell voltage of 0.004 V). For open chamber testing, experiments at low speed and low load (LSLL) and high speed and high load (HSHL) were conducted at nominal and advanced sparking timing (NS and AS, respectively). Figure 27 shows the OC configuration on the Ajax engine with the Champion W18 spark plug screwed in and the ignition connected.

Figure 27: OC configuration on Ajax E-565 engine.

The Ajax E-565 has nominal spark timing of 11.5 degrees before top dead center (BTDC), with advanced spark timing set to 16.5 degrees BTDC (advanced 5 degrees) using the Altronic ignition system software (Figure 28). Note that 11.5 and 16.5 degrees BTDC are equivalent to -11.5 and -16.5 degrees after top dead center (ATDC).

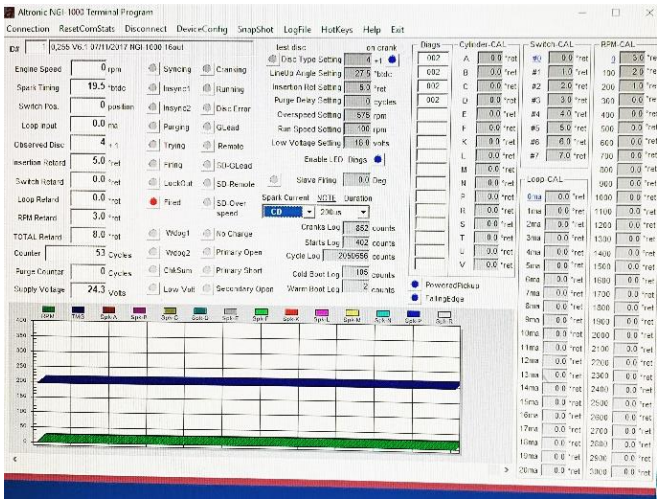

Figure 28: Altronic NGI-1000 system software.

All OC experiments were conducted on October 26, 27, and 28 in 2020. Data was collected using AERL's "AjaxGetData" function in Matlab. Air flow measurements were collected manually from a manometer connected to a laminar flow element. Example data is shown below in Table 4. Note, for example, that OCHSHLNS102620 in Table 4 means Open Chamber High Speed High Load at Nominal Spark Timing, conducted on October 26, 2020.

Table 4: Example data set from OC experimentation (blue shaded tiles are constants).

	OCHSHLAS102820	OCLSLLNS102620
Speed (RPM)	500.17	434.30
Load (V)	0.004	0.0025
Ign. Timing (deg-btdc)	16.5	11.5
Amb. Temp. (K)	300	303
Intake Temp. (K)	309.15	318.91
Exh. Temp (K)	682.65	673.87
Manometer (in. water)	2.45	2.2
Fuel Flow Rate (SLPM)	158.72	109.76

After data was collected from each OC experiment (HSHLAS, LSLLNS, etc.), the data was averaged for each corresponding experiment after post-processing. For example, all OCHSHLAS tests conducted on October 26, 27, and 28 were averaged into one data set with calculated uncertainties. Post-processing takes the data measured in volts and outputs it into units that can be easily read and used for calculations. The engine performance parameters are calculated below in section *3.3. Engine Data Collection and Calculations*.

3.2.2. Prechamber Testing

The procedure for running the engine and collecting data with the prechambers is the same as OC operation, with exception to how fuel is supplied. First, the high-pressure valve and the ball valve just before the fuel regulators on the PCC fuel line were turned to the open position. Next, as "Push to Start" is held on the ignition box and the flywheel is spinning, fuel is throttled into the main chamber's direct injection system as another researcher slowly opens the ball valve that releases natural gas into the PCC line. Once the engine is running with the prechamber, data can be collected in the same manner as OC testing. Table 5 shows sample data from PCC testing.

Table 5: Example data set from PCC experimentation (blue shaded tiles are constants).

	P2HSHLAS102720	P3HSHLAS102820
Speed (RPM)	505.84	504.71
Load (V)	0.004	0.004
Ign. Timing (deg-btdc)	16.5	16.5
Amb. Temp. (K)	298.81	298.44
Intake Temp. (K)	307.38	312.56
Exh. Temp (K)	674.53	681.15
Barometer (in. fluid)	2.5	2.45
Fuel Flow Rate (SLPM)	169.85	175.56
PCC Fuel Pressure (psia)	23	23

P1 was tested on October 26 and 27, 2020, P2 was tested on October 26 and 27, 2020, and P3 was tested on October 27 and 28, 2020. Figure 29 shows the prechambers screwed into the MCC. The black hoses are the water lines, which pump water through the PCC to keep it cool during operation. The red and white plug is the ignition starter, which is connected to the ignition box. Lastly, the steel hose provides fuel to the PCC. There is ample insulation to ensure the heat from the exhaust does not overheat the fuel or water lines.

Figure 29: P1 (left), P2 (middle), and P3 (right) installed on the Ajax E-565 engine.

3.3. Engine Data Collection and Calculations

Post-processed data was used to calculate the following engine performance parameters: peak pressure, IMEP, coefficient of variation in IMEP (COV_{IMEP}), location of peak pressure (LoPP), fuel flow rate, mass of fuel per cycle (m_{fuel}/cycle), crank angle at which 50% of combustion heat has been released (CA-50), combustion duration, flame development angle, rate of heat release (ROHR), mass fraction burned (MFB), indicated fuel conversion efficiency ($\eta_{f,i}$), combustion efficiency (η_c), brake fuel conversion efficiency ($\eta_{f,b}$), and brake thermal efficiency ($\eta_{t,b}$). Data from the Horiba emissions bench was used to calculate the following emissions parameters: BSCO, $BSNO_x$, BSTHC, $BSCO_2$, and BSO_2. Nontrivial calculations are shown below.

3.3.1. Pressure

In-cylinder pressure versus crank angle (in 0.25-degree increments) is measured as a voltage at the intake and exhaust with piezoresistive pressure sensors and then calibrated in Matlab from volts to kPa. IMEP was calculated by using equation (8), where P is the pressure at a given crank angle, dV is the change in volume from one crank angle increment to the next, and V_d is the total displaced volume. Thus, IMEP is the work output for the engine cylinder's swept volume, independent of the engine's speed, number of cylinders, and displacement [52].

$$IMEP = \sum \frac{PdV}{V_d} \tag{8}$$

COV_{IMEP} is the standard deviation of IMEP (σ_{IMEP}) divided by the average IMEP (μ_{IMEP}), shown in equation (9). COV_{IMEP} is an indication of the variation of work output, or combustion variability, with higher stability at lower values of COV_{IMEP}.

$$COV_{IMEP} = \frac{\sigma_{IMEP}}{\mu_{IMEP}} \tag{9}$$

3.3.2. Mass Fraction Burned

Rate of heat release (ROHR) reveals how much energy is released by the fuel during the combustion stroke of the engine from spark ignition to exhaust port opening (EPO), or from spark initiation to when ROHR starts to settle at around zero [53]. ROHR and the cumulative amount of heat release is used to control parameters such as fuel economy, emissions, and noise.

ROHR is defined by equation (10), which is Heywood's simplified definition of ROHR [8], using the following assumptions: constant mass, chemical equilibrium for burned gases, no change in residual fraction [53], no effect of crevice flow and blow-by due to imperfect sealing [8], constant R (though single-zone modeling is not as accurate as multi-zone modeling [53]), constant specific heat (though mass fraction burned [MFB] may vary by up to 10% [8]), and no heat loss to the walls [8]. In equation (10), γ is the ratio of specific heats, P is pressure, dV is change in volume, V is volume, and dP is change in pressure.

$$ROHR = \left(\frac{\gamma}{\gamma - 1}\right) PdV + \left(\frac{1}{\gamma - 1}\right) VdP \tag{10}$$

MFB is a function of crank angle, and is the amount of fuel-air mixture burned during the combustion process, normalized from 0 to 1 MFB (0% to 100% mass burned). Each test point was normalized to reach 100% mass burned, though combustion efficiency was less than 100%. End of combustion was determined by a ROHR reaching zero. MFB is defined by equation (11), where ϑ is crank angle, ϑ_{spark} is the crank angle at which spark is ignited, and ϑ_{EOC} is the crank angle at the end of combustion (EOC).

$$MFB(\theta) = \frac{\int_{\vartheta_{spark}}^{\vartheta} ROHR \, d\vartheta}{\int_{\vartheta_{spark}}^{\vartheta_{EOC}} ROHR \, d\vartheta} \tag{11}$$

0% to 10% MFB defines the flame initiation period, and 10% to 90% MFB defines the rapid burning period. The MFB and ROHR profiles control the shape of the in-cylinder pressure curve, which controls how much work is transferred by the engine cycle and, thus, the engine's torque.

3.3.3. Efficiencies

Fuel conversion efficiency is the ratio between the engine's useful mechanical work and the fuel energy per cycle, and is an indication of the engine's usable fuel energy [8]. Indicated fuel conversion efficiency ($\eta_{f,i}$) is derived at the flywheel, whereas brake

parameters are obtained by breaking the free rotation of the crankshaft using a dynamometer and applying a load. Thus, brake fuel conversion efficiency is slightly lower than indicated fuel conversion efficiency because brake fuel conversion efficiency includes friction losses and all losses up to the crankshaft. Indicated fuel conversion efficiency was calculated using equation (12), where the product of μ_{IMEP} and V_d is net indicated work per cycle, m_{fuel} is the mass of the fuel, and Q_{LHV} is the lower heating value of methane.

$$\eta_{f,i} = \frac{\mu_{IMEP} * V_d}{m_{fuel} * Q_{LHV}} \tag{12}$$

Brake fuel conversion efficiency was calculated by taking brake power (which is equal to the product of brake work per revolution and RPM), and dividing by the product of fuel flow and lower heating value of methane. Note that brake work per revolution is equal to $2\pi\tau_b$, where τ_b is brake torque. Brake fuel conversion efficiency was calculated using equation (13), where $\dot{m}_{fuel}$ is the mass flow rate of fuel.

$$\eta_{f,b} = \frac{2\pi\tau_b * RPM}{\dot{m}_{fuel} * Q_{LHV}} \tag{13}$$

Combustion efficiency is the fraction of heat released by the fuel during combustion to the energy supplied by the fuel [8]. After every combustion reaction, exhaust products are produced that consist of incomplete and complete combustion

products. Fewer incomplete combustion products are produced under lean operating conditions than when the air-fuel mixture is rich. Combustion efficiency measures how well the burned fuel is being used during the combustion process, and was calculated by dividing the heat release by the fuel energy and subtracting by 1, shown in equation (14). Heat release (Q_{out}) was determined by multiplying the wet fractions of incomplete products (H_2, CO, and THC) by their respective heating values and molecular weights, and then summing them together. The heat release was then divided by the total molecular weight of the incomplete products. The energy of the fuel (E_{fuel}) was determined by multiplying the ratio of fuel flow to fuel and air flow by the lower heating value (LHV) of the fuel (the LHV of the fuel used was 47.141 MJ/kg).

$$\eta_c = 1 - \frac{\left(\frac{Q_{out}}{MW_{mix}}\right)}{E_{fuel}} \tag{14}$$

Brake thermal efficiency ($\eta_{t,b}$) is one of the most important measures when comparing efficiencies between engines. Brake thermal efficiency evaluates how well heat is converted from fuel to mechanical energy [54] by removing the effects of incomplete combustion and relating work per cycle to fuel chemical energy released during combustion [8]. Brake thermal efficiency was calculated by dividing brake fuel conversion efficiency by combustion efficiency, shown in equation (15).

$$\eta_{t,b} = \frac{\eta_{f,b}}{\eta_c} \tag{15}$$

3.3.4. Brake Specific Emissions

Brake specific emissions evaluate engine emissions (NO_x, THC, CO, CO_2, etc.) relative to how much useful work is produced by the engine (including how much mass is flowing through the engine), providing a more complete accounting for emissions compared to just observing emission concentrations. Brake specific emissions were calculated by taking the wet concentration of the measured emission (ex: $NO_{x,w}$), multiplying the wet concentration by its molecular weight (ex: MW_{NO_x} of 46.01 g/mol or MW_{THC} of 16.04 g/mol) and the total exhaust mass ($m_{exh} = m_{fuel} + m_{air}$), then dividing by the product of the total molecular weight of the exhaust (MW_{exh}) and the engine's horsepower (hp). The result is brake specific emissions in g/hp-hr. Equation (16) is an example using NO_x to calculate $BSNO_x$, but the equation can be applied to any brake specific emission.

$$BSNO_x = \frac{NO_{x,w} * MW_{NO_x} * m_{exh}}{MW_{exh} * hp} \tag{16}$$

4. RESULTS AND DISCUSSION

4.1. Low Speed and Low Load

Low speed and low load (LSLL) conditions were conducted at 430 RPM (Figure 30) and 65% load, respectively. P1, the SIP previously tested by Cooper Machinery Services on an Ajax E-42, could not be tested at higher speeds or loads. Initially, P1 had difficulty firing and maintaining consistent combustion, so the 0.019" orifice was installed into the check valve to provide the largest range of pressure and fuel flow. P1 started to fire successfully, but required slow fuel addition into the PCC and MCC in order to reach 430 RPM at 65% load. At higher speeds or loads, the Ajax E-565 engine would stop running altogether. At LSLL conditions, P1 frequently experienced a misfire cycle followed by an abnormally intense fired cycle, such that combustion occurred every four strokes instead of every two strokes. This is colloquially known as "four-stroking" in the pipeline compressor engine industry, although of course the cylinder is still experiencing gas exchange with every revolution of the crankshaft.

As the engine was operating at a lower speed and load, the engine could not fire stably with P1. The engine was tested with an OC configuration at LSLL to compare performance and emissions results with P1. Just as it was for Cooper Machinery Services on their Ajax E-42, P1 was difficult to run on the Ajax E-565 and could never reach consistent combustion each cycle. Stable combustion could not be reached at either nominal or advanced spark timing. When spark timing was retarded, P1 could not fire altogether. Poor combustion and ignition instability are partially due to P1's Craya-Curet

number of approximately 0.122 at the spark plug ignition region and 0.180 at the nozzle outlet. According to Olsen et al., a C_t of less than 0.2 results in poor ignition, with 0.3 being optimal [4].

4.2. High Speed and High Load

High speed and high load (HSHL) conditions were conducted at 500 RPM (Figure 30) and 100% load, respectively. P2 and P3 were both able to successfully operate at HSHL conditions with stable combustion. P2 and P3 were combusting during most cycles, whereas P1 at LSLL and OC at LSHL did not. P2 and P3 were both tested at nominal and advanced spark timing. When retarding the spark timing, in each case the engine would run for approximately 30 seconds and then stop firing. The results and discussion below reveal and explain the performance and emission results between P1, P2, P3 and OC operation.

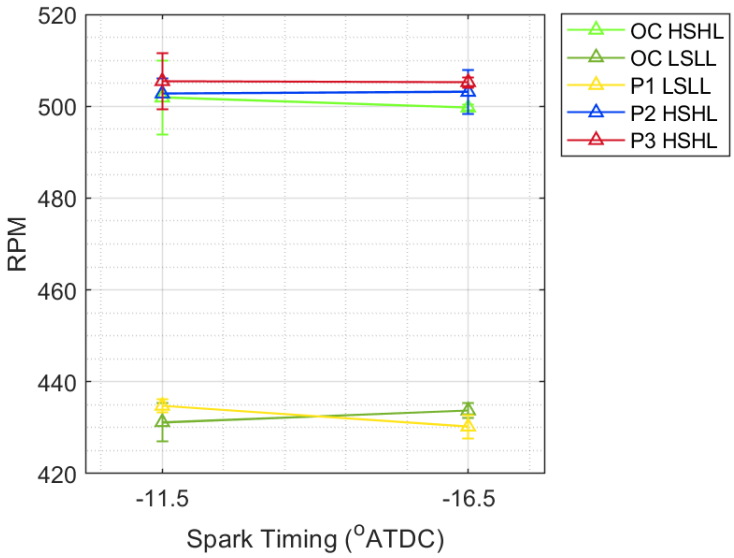

Figure 30: Crankshaft speed (RPM) at -11.5 and -16.5 °ATDC spark timings for OC and PCCs at varying speed and load.

4.3. Pressure

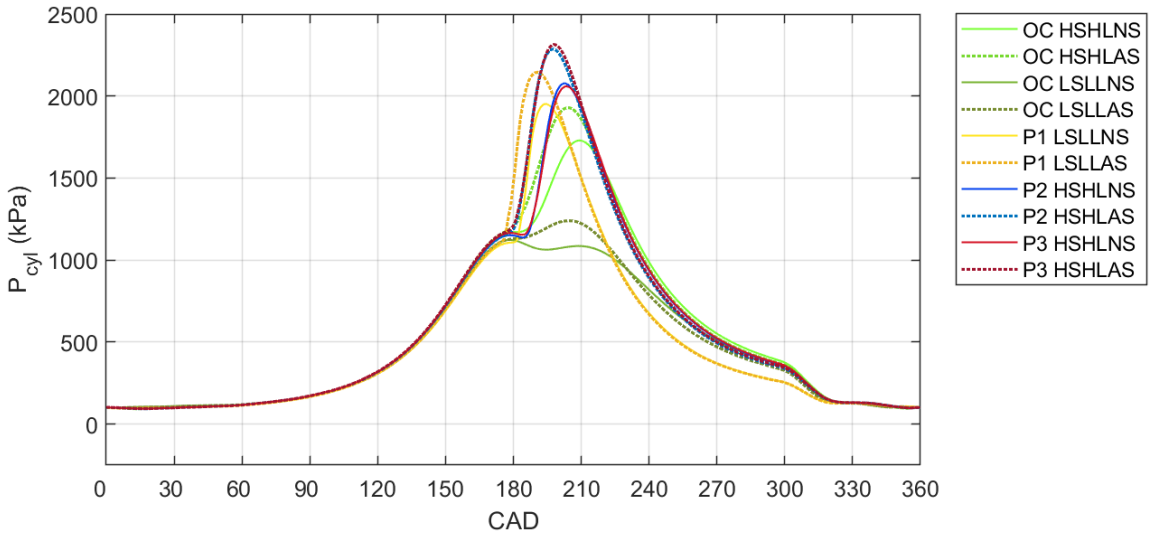

Figure 31: In-cylinder pressure (P_{cyl}) traces vs. crank angle degree (CAD) for OC and PCCs at varying speed, load, and spark timing.

Figure 31 shows the pressure traces for the averaged test cycles (OC test conditions were conducted three times each, then averaged; PCC test conditions were conducted two times each, then averaged). At any condition, LSLL or HSHL, the peak pressure was higher for PCC operation than for OC operation, which is further evidenced in Figure 32. The Ajax E-565 engine experienced much higher pressures when operating with a PCC than with OC due to the PCC's much smaller area and volume ejecting an explosive jet into the MCC, an increased burn rate, and the four-stroking phenomenon on the averaged cycles. The increased pressure inside of the PCC ejected a jet into the MCC, which would typically allow the MCC to operate with much leaner fuel-air mixtures, but was not the case in this study (discussed in further detail below). P1 obtained the largest rise in peak pressure compared to OC operation at LSLL, with an increase of 67.2% at nominal spark timing and 63.5% at advanced spark timing. P2 experienced a 24.0% and 21.1% increase in peak pressure at nominal spark timing and advanced spark timing, respectively, compared to OC operation at HSHL (Figure 32). P3 experienced a 22.2% and 22.6% increase in peak pressure at nominal spark timing and advanced spark timing, respectively, compared to OC operation at HSHL (Figure 32). Higher pressure rises allow for higher work output and torque.

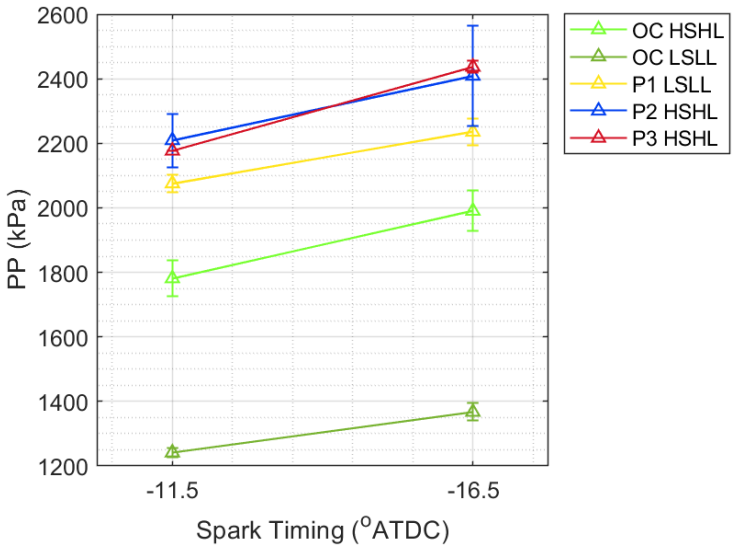

Figure 32: Peak pressure (PP) at -11.5 and -16.5 °ATDC spark timings for OC and PCCs at varying speed and load.

When advancing spark timing by 5 CAD, peak pressures are higher compared to peak pressures at nominal spark timing. Increased peak pressures are a result of starting the heat release process sooner by advancing the spark timing. ROHR appears to be slightly lower for each advanced ignition case, which indicates that the higher peak pressures in Figure 32 are a result of changing the phasing of combustion rather than the speed. The pressure traces also reveal how quickly pressure rises when operating with PCCs, as all pressure traces with a PCC have a steeper rise in pressure compared to OC operation. Steeper rises in pressure are a result of ROHR and MFB, which are discussed in further detail in section *4.5. Mass Fraction Burned*.

Figure 33 shows that at both spark timings and HSHL conditions, LoPP was approximately 8 CAD earlier for P2 and P3 than for OC. Thus, P2 and P3 at nominal spark timing and OC at advanced spark timing, all at HSHL, have similar combustion

phasing earlier in the MFB curve (Figure 39). For the remainder of this study, P2 and P3 at nominal spark timing and OC at advanced spark timing will be compared to evaluate performance and emissions in greater depth.

As spark timing is advanced, the LoPP is also advanced, with exception to OC at LSLL (Figure 33). For OC at LSLL, nominal spark timing resulted in a higher peak pressure due to compression rather than combustion, which is further evidenced in Figure 31. Thus, LoPP for OC at LSLL and advanced timing increases because it is achieving more stable combustion with a contribution to peak pressure from both compression and combustion. Normally, LoPP for OC at LSLL and nominal spark timing would be higher, resulting in a decrease in LoPP with advanced spark timing. However, pressure peaked due to compression at LSLL and nominal spark timing for OC, with a lower peak pressure due to combustion.

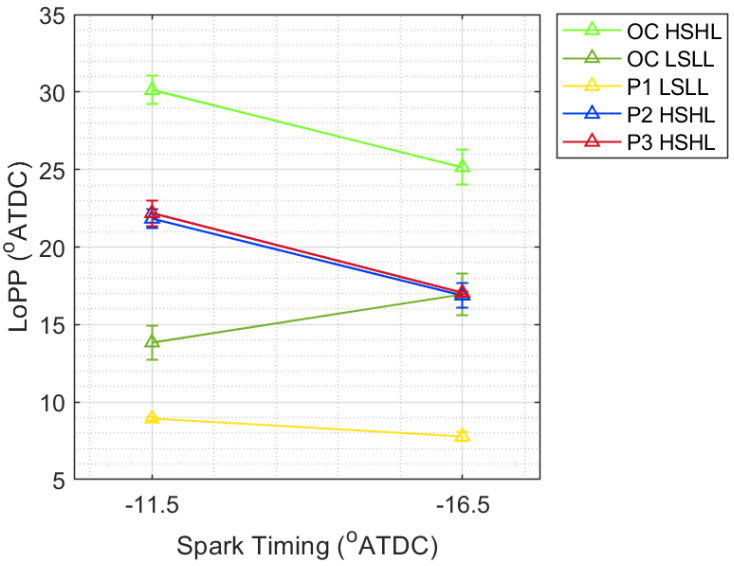

Figure 33: Location of peak pressure (LoPP) at -11.5 and -16.5 °ATDC spark timings for OC and PCCs at varying speed and load.

As stated previously, IMEP is the work output for the engine cylinder's swept volume, independent of the engine's speed, number of cylinders, and displacement. Figure 34 shows that at LSLL, P1 had a lower IMEP than OC operation at both spark timings. P1's IMEP is lower than OC even though its peak pressure is much higher, which may be revealed in the ROHR plots (Figure 38), as ROHR peaks early for P1 then slowly releases heat through the rest of the cycle. Thus, P1 is less efficient in producing work than OC operation. P2, P3, and OC at HSHL have overlapping error bars, which indicates no statistical difference between IMEP at HSHL. The higher IMEP is a result of higher in-cylinder pressures, which indicates that the flame initiation period is longer. The higher IMEP is governed primarily by burning more fuel, causing a higher load, and phasing that combustion event well enough. There are not important differences in IMEP among P2, P3, and OC at HSHL (Figure 34), though the ROHR plots were different.

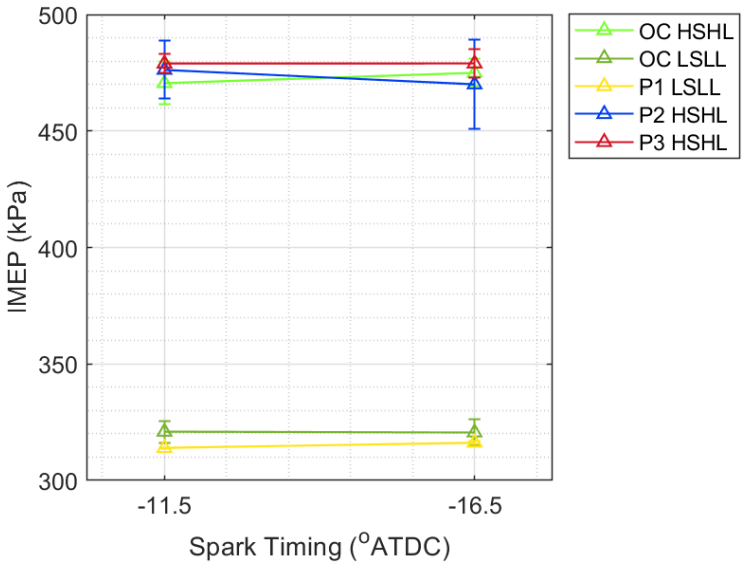

Figure 34: Indicated mean effective pressure (IMEP) at -11.5 and -16.5 °ATDC spark timings for OC and PCCs at varying speed and load.

COV_{IMEP} is an indication of combustion variability, with higher stability at lower values of COV_{IMEP}. Figure 35 shows that P1 had the lowest engine stability, with an increase of 7.93% in engine stability when spark timing is advanced. For P2, P3, and OC at HSHL and OC at LSLL, engine stability decreased with advanced spark timing by 2.84%, 4.65%, 1.79%, and 16.64%, respectively (Figure 35). However, COV_{IMEP} for P2 and P3 at advanced spark timings were within the error bars at nominal spark timing, indicating that engine stability was not much worse at advanced spark timing for P2 and P3. At nominal and advanced spark timing, OC at HSHL achieved the most stable engine operation. Of the HSHL test conditions, P3 was the least stable at both spark timings, with a decrease of 77.9% and 75.8% from OC at nominal and advanced spark timing, respectively. At HSHL, P2 was in the middle in terms of engine stability, decreasing in stability by 72.2% and 69.7% compared to OC at nominal and advanced spark timing, respectively. However, overlapping uncertainty between P2 and P3 at nominal spark timing indicates no statistical difference in the data as uncertainty was calculated with a 95% confidence interval. P2 achieved a more stable engine operation than P3 at advanced spark timing, and a statistically equivalent engine stability at nominal spark timing. OC at LSLL achieved approximately the same engine stability as P2 at nominal spark timing and better stability than P3; therefore, P2 and P3, which ran at 500 RPM and full load, were just as stable or less stable than the engine operating with an OC configuration at LSLL and nominal spark timing, normally an inefficient condition. At advanced spark timing, OC at LSLL achieved a much lower engine stability, decreasing by 40.8%. Thus,

at advanced spark timing, P2 and P3 achieved a more stable operating condition than OC at LSLL.

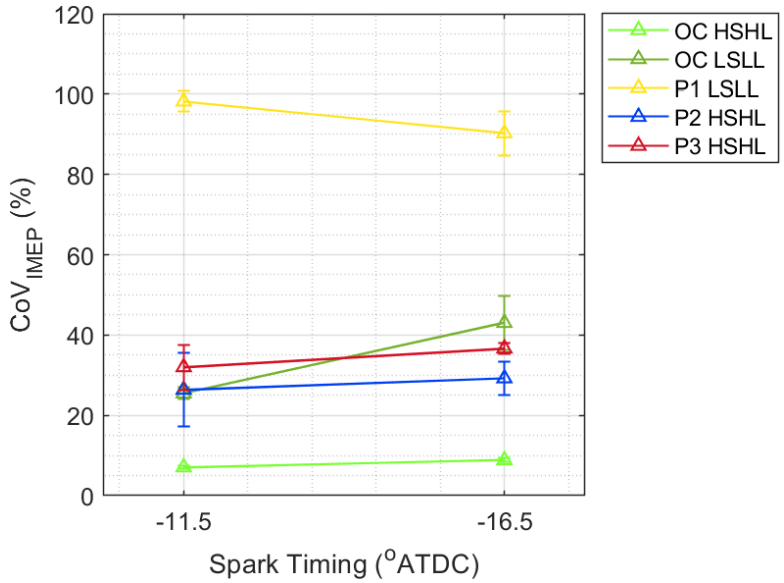

Figure 35: Coefficient of variation of IMEP (COV_{IMEP}) at -11.5 and -16.5 °ATDC spark timings for OC and PCCs at varying speed and load.

Overall, the PCCs increased peak pressure per cycle compared to OC operation. P2 and P3 at HSHL operated with worse stability than OC at HSHL, and P1 at LSLL also operated with worse stability than OC at LSLL. At nominal spark timing, P2 and P3 at HSHL have statistically the same COV_{IMEP} as OC at LSLL. P2 and P3 achieved more stable engine operation than OC at LSLL with advanced spark timing. Engine stability decreased at nominal spark timing by 72.2% and 77.9% when using P2 and P3, respectively, compared to OC operation at HSHL and nominal spark timing. At advanced spark timing, P2 and P3 decreased engine stability by 69.7% and 75.8%, respectively. Lastly, P2 and P3 at nominal spark timing have similar combustion phasing to OC at

HSHL and advanced spark timing, but are 66.4% and 72.3%, respectively, less stable than the OC configuration.

4.4. Fuel Consumption

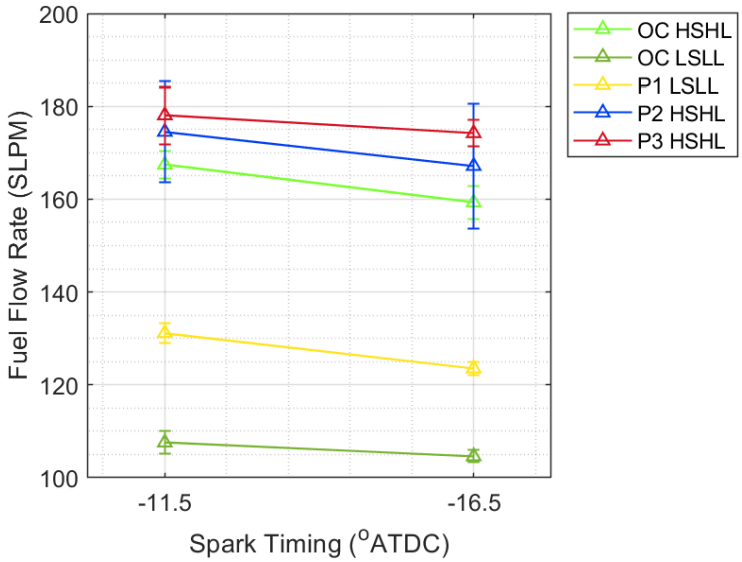

Figure 36: Fuel flow rate at -11.5 and -16.5 °ATDC spark timings for OC and PCCs at varying speed and load.

Fuel flow rate decreased for all OC and PCC test conditions when spark timing was advanced, shown in Figure 36. At LSLL, P1 had a fuel flow rate of 131.2 SLPM and 123.5 SLPM at nominal and advanced spark timing, respectively. OC at LSLL had a fuel flow rate of 107.6 SLPM and 104.6 SLPM at nominal and advanced spark timing, respectively. Thus, OC at LSLL had a 18.0% and 15.3% lower fuel flow rate than P1 at nominal and advanced spark timing, respectively. The lower fuel flow rate corresponded to a 17.3% and 16.0% decrease in mass of fuel consumed per cycle by the OC configuration at LSLL and nominal and advanced spark timing, respectively (Figure 37).

P2 and P3 also consumed more mass of fuel than OC at HSHL, with P3 consuming the most fuel. Though uncertainty between OC at HSHL and P2 at nominal and advanced spark timing overlaps, no overlap in uncertainty occurs between OC at HSHL and P3 at advanced spark timing. Thus, P3 definitively consumed more fuel per cycle than OC at HSHL at both spark timings.

With P2 and P3 at HSHL and nominal spark timing and OC at HSHL and advanced spark timing having an LoPP near each other, comparing the fuel consumed per cycle for those conditions given their similar combustion phasing was useful. Figure 37 shows that P3 at nominal spark timing still consumed 9.50% more fuel than OC at advanced spark timing. P2 at nominal spark timing consumed 8.13% more fuel than OC at advanced spark timing. The PCCs that consumed more fuel compared to their HSHL or LSLL OC counterparts is counterintuitive for how the PCC is supposed to operate. Normally, we would expect reduced fuel consumption in the MCC with a PCC installed as the PCC would allow the MCC to operate at much leaner fuel-air conditions. In a study by Slefarski et al., the GMVH-12 natural gas engine used to operate Eco-Jet prechambers (P2 and P3 in this study) operated with a fuel system pressure of 30.5 psi to 50.8 psi and reduced specific fuel consumption by 7% [55].

Moreover, in a study by Olsen et al., prechambers with a length to diameter ratio of less than 1.5 have a severely worse mixing process, and a C_t of less than 0.2 results in poor ignition [4]. Table 2 shows that P1 had an L/D ratio of 1.07 at the spark plug inlet and 1.48 at the nozzle outlet; P2 had an L/D ratio of 1.37; and P3 had an L/D ratio of 1.38. Thus, all prechambers were below the minimum L/D design requirement for an optimal

mixing process. P1 had the worst L/D ratio of 1.07 where spark occurs, resulting in the worst mixing process. C_t for P1 was 0.122 at the spark plug inlet and 0.180 at the nozzle outlet, for P2 the C_t was 0.147, and for P3 the C_t was 0.178. Craya-Curtet numbers should be between 0.22 and 0.3, with 0.3 being the most optimal [35].

The results of the L/D ratios and Craya-Curtet numbers explain the mass of fuel used per cycle in Figure 37. P1 had the worst fuel-air mixing; thus, in order to reach the same speed of 430 RPM and 62.5% load as OC at LSLL, P1 needed to consume more fuel than the OC configuration due to its poor mixing process. P3 had the worst mixing process of the HSHL configurations, which is why it consumed the most fuel out of P2 and OC at HSHL in order to reach maximum load at 500 RPM. Next was P2, which also consumed more fuel than OC at HSHL. How L/D ratio and C_t affected the engine's efficiency is discussed in section *4.6. Efficiencies*.

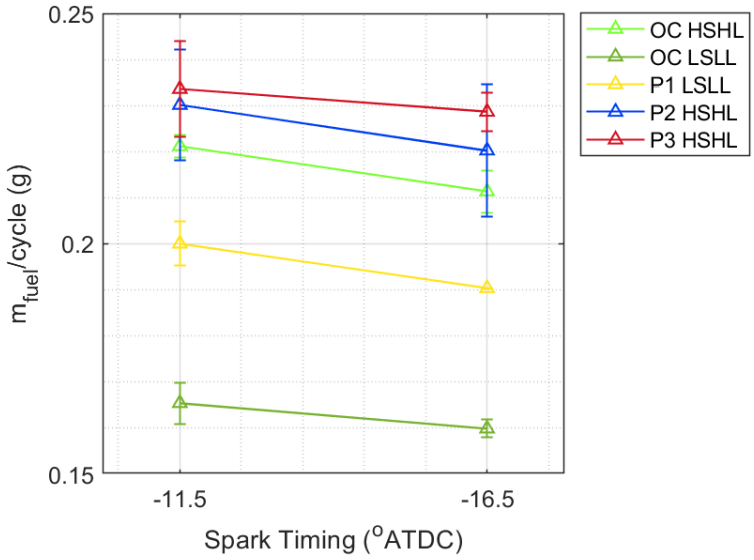

Figure 37: Mass of fuel per cycle (m_{fuel}/cycle) at -11.5 and -16.5 °ATDC spark timings for OC and PCCs at varying speed and load.

4.5. Mass Fraction Burned

As previously discussed, ROHR is the apparent rate of heat released in the cycle. In Figure 38 for ROHR with PCC and OC configurations, the initial rise in ROHR is the start of combustion after flame initiation. For all test conditions, advancing spark timing resulted with ROHR shifting left with a lower peak. For both spark timings, the actual burning rates in the engine are similar; however, the calculated net ROHR has no heat transfer model, so it may not be capturing the additional heat lost to the walls when combustion occurs closer to TDC. The shift left is a result of combustion occurring sooner due to advanced spark timing with a lower relative volume due to piston positioning. Figure 31 shows peak pressures are much higher for experiments at advanced spark, which is a result of the combustion phasing. P2 also has a higher peaked ROHR curve than P3, which is a result of mass being burned faster during combustion. Higher ROHR in P2 could be due to higher turbulence intensity or a more homogeneous mixture at that speed, though differences between ROHR for P2 and P3 were small. P3 also had an off-axis nozzle, which could have contributed to slight differences that were seen in combustion.

At a more advanced spark timing, the apparently lower ROHR curves could be a result of a slightly leaner fuel composition. With a mixture slightly lean of stoichiometric, the laminar flame speed will produce lower flame temperatures. Reduced ROHR curves at more advanced spark timings may also be a result of poor engine tuning. By advancing spark ignition, the timing of the compressive and expansive parts of the sound waves entering the intake port and exiting the exhaust port change, which affects the tuning of the engine. The result of the higher peaked ROHR for P2 compared to any other test

condition, at nominal or advanced spark timing, may also be a result of a change in its fuel-air mixture, resulting in higher turbulence intensity and entrainment rate. Note that ROHR is calculated and does not add heat losses back in order to find the actual burning rate; thus, the apparently lower ROHR curves may be a result of the shortcomings of the net ROHR calculation.

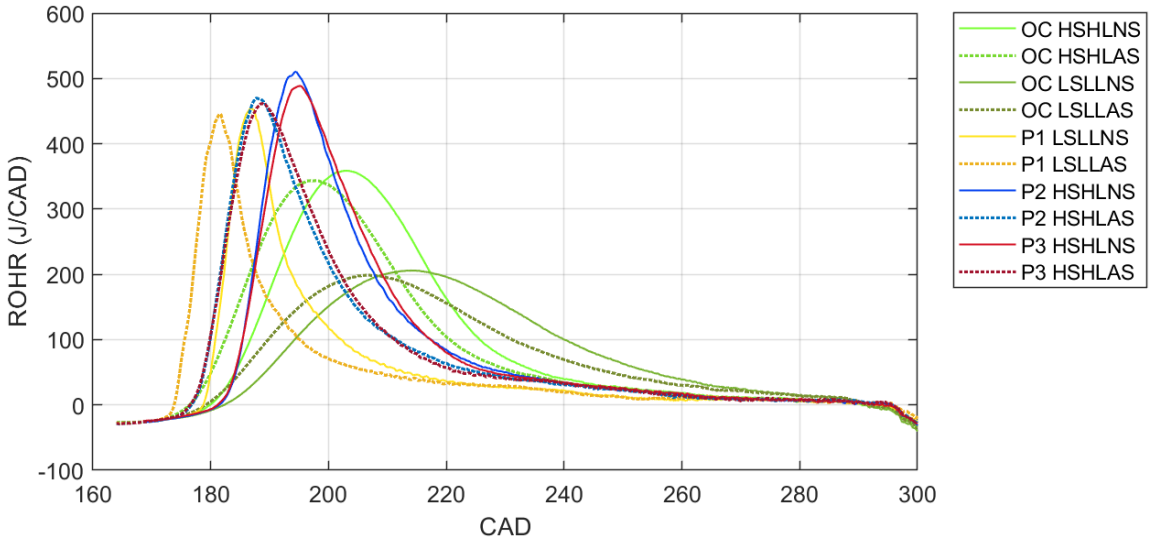

Figure 38: Rate of heat release (ROHR) vs. crank angle degree (CAD) for OC and PCCs at varying speed, load, and spark timing.

MFB characterizes the amount of fuel-air mixture being burned during the combustion process with respect to the total fuel-air mixture available before combustion occurs. MFB is a function of crank ankle, normalized from 0 to 1. The region from 0 to 0.1 MFB defines the flame initiation period and 0.1 to 0.9 defines the rapid burning period. As the shape of the MFB curve changes, the in-cylinder pressure curve changes accordingly, which dictates the amount of work produced by the engine.

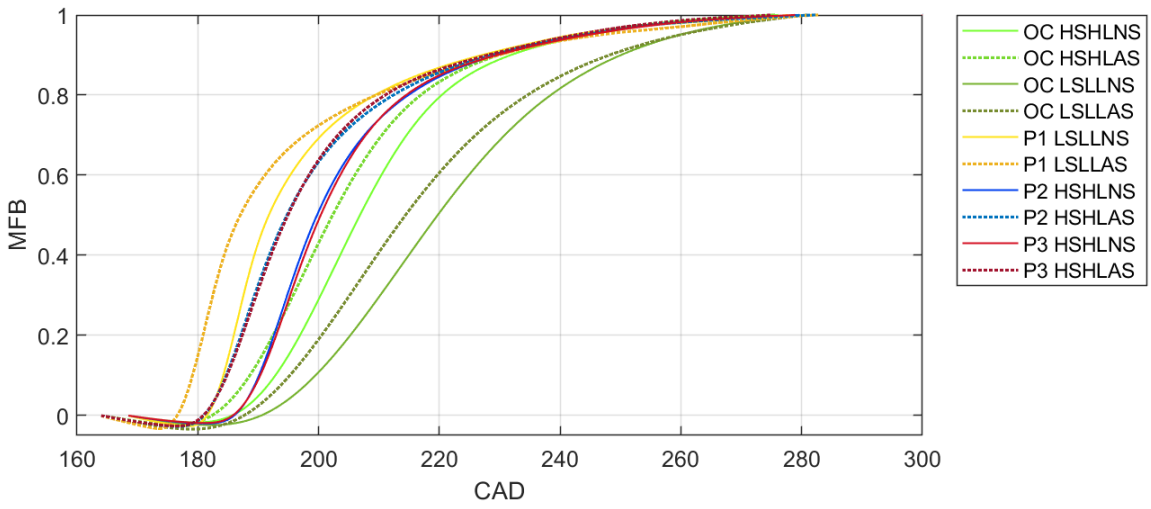

Figure 39: Mass fraction burned (MFB) vs. crank angle degree (CAD) for OC and PCCs at varying speed, load, and spark timing.

As spark timing was advanced, the MFB curve shifted left for all test conditions (Figure 39). From P1 to P3, the MFB curve shifted right. On average, combustion duration increased slightly with advanced spark timing (Figure 40), which shows that fuel is being burned slower due to changes in in-cylinder properties (such as laminar flame speed, turbulence intensity, unburned mixture density, and burn up time). A slight increase in combustion duration may also be attributed to the missing heat transfer in ROHR; if ROHR were steeper near TDC, then 90% MFB would be achieved sooner, which would account for the small difference in combustion duration. P2, P3, and OC at HSHL had approximately the same combustion duration at advanced spark timing, but P2 and P3 has a slightly faster combustion duration than OC at nominal spark timing (Figure 40). P1 had the slowest combustion duration of 65.7 CAD and 61.2 CAD at nominal and advanced spark timing, respectively. At nominal spark timing, P1 had a significant range of uncertainty, which further demonstrates the poor combustion stability at that spark

timing. The combustion duration for P2, P3, and OC at HSHL were roughly the same at nominal and advanced spark timing, all falling within their ranges of uncertainty.

Additionally, flame development angles for OC conditions increased at advanced spark timing, while flame development angles decreased for the PCCs with advanced spark timing (Figure 41). Increased flame development angles correspond to a steeper slope, which indicates slower flame propagation. All PCCs achieved steeper MFB slopes at nominal and advanced spark timings, indicating faster flame propagation. Faster flame propagation could be a result of a more homogeneous mixture, turbulence intensity from the PCC's jet, and from an increase of 10^6 in ignition energy from the PCC. Turbulence intensity tends to increase with advanced spark timing in a spark-ignited engine [56]. Turbulence enhances combustion because it creates small packets of eddies that rotate as vortices. Higher turbulence intensity will speed up eddy rotation and can therefore transfer the flame faster. The flame follows the path of the wrinkled line created by these rotating eddies and propagates through the mixture and engulfs the eddies. The flame is short-circuiting itself along the lines built within the mixture. After turbulent entrainment, the eddies burn from the outside in, called the burn up period (0.1 to 0.9 mfb). These vortices allow the mixtures to burn faster than one stroke of an engine, allowing for higher pressure rises and, thus, higher work output and torque. Though the PCCs achieve a higher work output, they are not more efficient than operating the engine with an OC configuration due to increased fuel consumption. Efficiencies will be discussed in further detail in section *4.6. Efficiencies*.

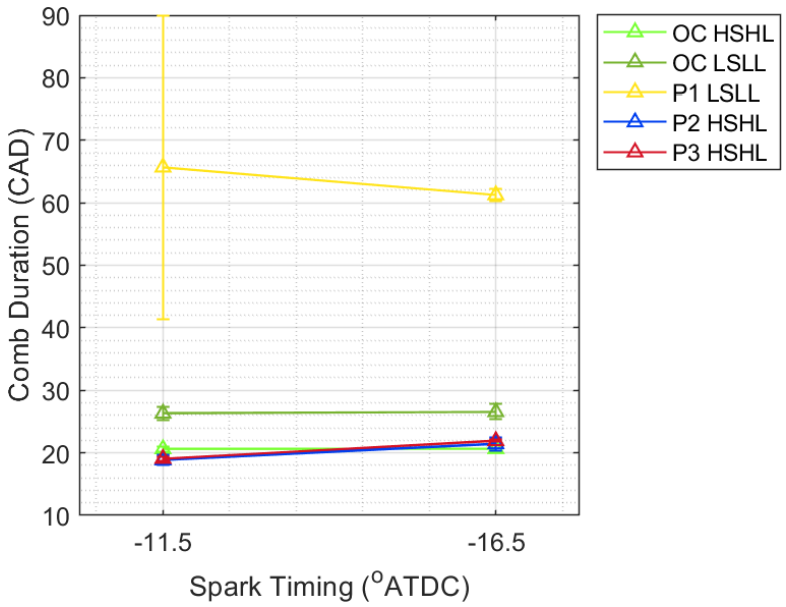

Figure 40: Combustion duration at -11.5 and -16.5 °ATDC spark timings for OC and PCCs at varying speed and load.

Under OC configured engine operation, flame development angles increased with advanced spark timing, but OC flame initiation was always longer than that of the PCC configurations. The steeper flame initiation period resulted in faster flame propagation. Under PCC engine operation, fuels burn faster with advanced spark timing because turbulence intensity increases with advanced spark timing as combustion occurs earlier than TDC, whereas turbulence intensity would decrease with retarded spark timing. At retarded spark timings, flame thickness increases, and combustion is slowed because more charge is burned during the expansion stroke, when energy is being extracted from the cylinder contents [56]. During combustion, the burning jet is expelled from the PCC into the MCC, and the remaining fuel-air mixture burns during expansion. Combustion may have also sped up for PCCs at advanced spark timing as a result of the jet expelled from the PCC burning the fuel-air mixture earlier before the piston reached TDC. Though

ignition could be improved further for the PCCs since they have Craya-Curtet numbers of less than 0.2, ignition appears perform better for the PCCs than the OC configuration due to their shorter flame development angles (Figure 41).

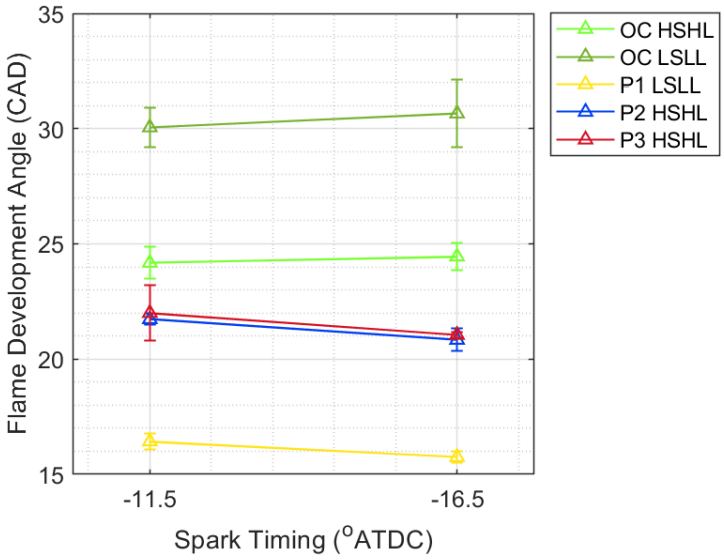

Figure 41: Flame development angle at -11.5 and -16.5 °ATDC spark timings for OC and PCCs at varying speed and load.

4.6. Efficiencies

Brake fuel conversion efficiency is an indication of the engine's usable fuel energy and includes all losses up to the crankshaft. At nominal spark timing, P1 experienced the lowest brake fuel conversion efficiency of 21.4% (Figure 42). OC at LSLL and nominal spark timing had an $\eta_{f,b}$ of 25.9%. Thus, $\eta_{f,b}$ for P1 was 4.50 percentage points lower than OC at nominal spark timing. At advanced spark timing, P1 was 4.29 percentage points lower than OC at LSLL. P2 and P3 were 1.23 and 1.69 percentage points lower, respectively, than OC at HSHL and nominal spark timing, and 1.33 and 2.53 percentage

points lower, respectively, than OC at advanced spark timing. All PCCs have poor ignition and mixing, resulting in lower brake fuel conversion efficiencies than operating the engine with an OC configuration. P1 has the lowest L/D ratio of 1.07 at the spark plug ignition site and 1.48 at the nozzle outlet, which resulted in the lowest brake fuel conversion efficiency. P2 and P3 had L/D ratios of 1.37 and 1.38, respectively, resulting in brake fuel conversion efficiency overlap due to the range of uncertainty. On average, P2 had higher brake fuel conversion efficiencies than P3 at both nominal and advanced spark timing.

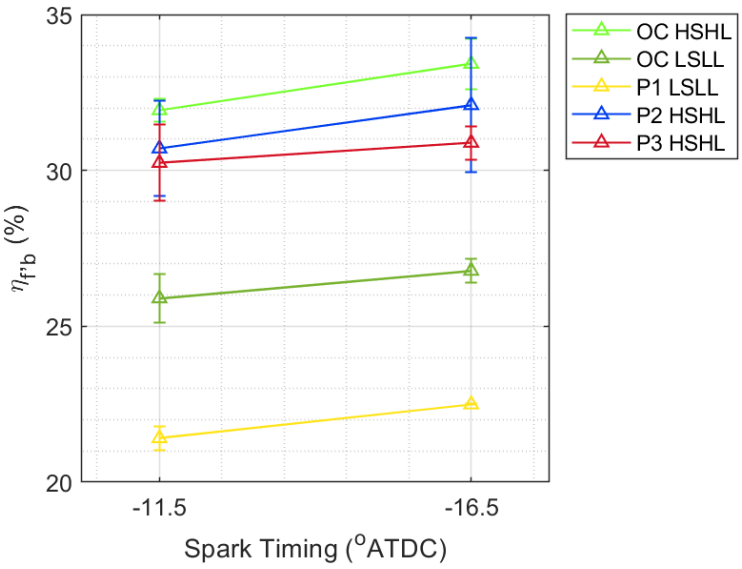

Figure 42: Brake fuel conversion efficiency ($\eta_{f,b}$) at -11.5 and -16.5 °ATDC spark timings for OC and PCCs at varying speed and load.

As spark timing was advanced, brake fuel conversion efficiency increased in all cases (Figure 42). When spark timing was advanced, less fuel was being consumed per cycle for all test conditions, shown in Figure 37. Additionally, IMEP stayed relatively

constant across nominal and advanced spark timing test conditions (Figure 34). Thus, work output stayed relatively constant with advanced spark timing and fuel consumption decreased with advanced spark timing, which resulted in an increase in brake fuel conversion efficiency for all test conditions.

As stated previously, combustion efficiency measures how well the burned fuel is being used during the combustion process. As ignition is not optimal for all PCCs due to low Craya-Curtet numbers, combustion efficiency was expected to be lower than for OC operation. Figure 43 shows that P1 had the worst combustion efficiency, with a combustion efficiency of 75.3% at nominal spark timing and 77.3% at advanced spark timing, which was 17.4 and 12.1 percentage points lower than OC at nominal and advanced spark timing, respectively, at LSLL. When spark timing was advanced, OC at LSLL had a reduced combustion efficiency, whereas P1 had a higher combustion efficiency.

Additionally, advanced spark timing resulted in an earlier rise in ROHR for P1, which resulted in a lower expansion pressure due to an earlier peak pressure (Figure 38). When spark timing is advanced, the combustion process starts earlier, and pressure rises due to both compression and combustion. While the peak pressure decreases, the late combustion raises the expansion pressure to higher levels than advanced spark timing does. The higher expansion pressures provide a stronger blowdown, which propagates down the exhaust and impacts the gas exchange performance. Thus, in the case for P1, advancing the spark timing improved engine stability by reducing COV_{IMEP} (Figure 35) and increased combustion efficiency (Figure 43) by positively altering the gas exchange

performance. Additionally, the "four-stroking" phenomenon causes misfires to expel additional HC emissions, which results in a partly scavenged cylinder. The next cycle then has a larger combustion event with possibly a richer mixture, leading to more HC emissions. Moreover, the combustion efficiency might be artificially deflated due to the four-stroking phenomenon. The four-stroking phenomenon would have caused emissions that would have otherwise not been able to participate in combustion, and the individual cycles in which combustion occurred must have higher combustion efficiencies than the average value that includes misfires.

Of the HSHL test conditions, P3 had the lowest combustion efficiency at both nominal and advanced spark timing (Figure 43), though P2's uncertainty completely overlapped all of the data points at nominal spark timing. At both nominal and advanced spark timing, OC at HSHL had higher combustion efficiencies than P2 and P3. At HSHL, P2's combustion efficiency was 2.39 and 2.45 percentage points lower than OC at nominal and advanced spark timing, respectively, and P3's combustion efficiency was 3.68 and 4.78 percentage points lower than OC at nominal and advanced spark timing, respectively. With improper mixing due to low L/D ratios and poor ignition due to low C_t numbers, combustion efficiency was lower for the PCCs than under normal OC operation. Combustion efficiency decreased for P3 with advanced spark timing, indicating that gas exchange performance declined, and engine's tune was poor with the spark advancement. Combustion efficiency stayed relatively constant for P2, and slightly increased for OC at HSHL. Additionally, combustion efficiency is a major factor in reducing PCCs fuel

conversion efficiency. Worse combustion efficiency usually corresponds to a worse fuel conversion efficiency, although that was not the case for OC at LSLL and P3.

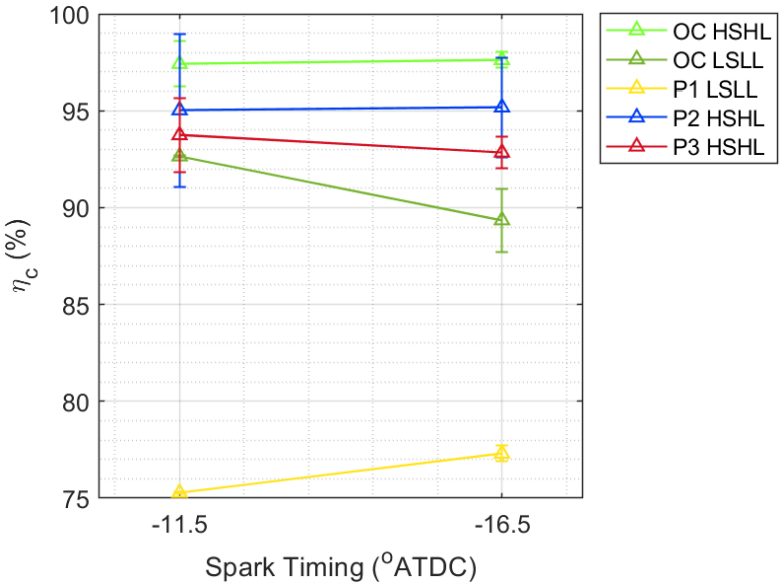

Figure 43: Combustion efficiency (η_c) at -11.5 and -16.5 °ATDC spark timings for OC and PCCs at varying speed and load.

As stated previously, brake thermal efficiency evaluates how well the energy released by combustion is converted to useful work [54] by removing the effects of incomplete combustion and relating work per cycle to the fuel chemical energy released during combustion [8]. Brake thermal efficiency is an important measure for engine performance. As shown in Figure 44, data uncertainty is greatly overlapped. However, overlap in uncertainty between OC at HSHL and P3 at advanced spark timing is minimal, which shows that OC at HSHL and advanced spark timing is observably more efficient than P3. On average, the brake thermal efficiencies follow similar trends to what has already been discovered. Thus, OC at HSHL achieved higher efficiencies than P2 and P3

at both nominal and advanced spark timing, with advanced spark timing being the most efficient. OC at HSHL had a brake thermal efficiency of 32.77% and 34.23% at nominal and advanced spark timing, respectively; P2 had a brake thermal efficiency of 32.26% and 33.72% at nominal and advanced spark timing, respectively; and P3 had a brake thermal efficiency of 32.26% and 33.27% at nominal and advanced spark timing, respectively. P2 was 0.51 and 0.51 percentage points lower in thermal efficiency than OC at nominal and advanced spark timing, respectively, and P3 was 0.51 and 0.96 percentage points lower in thermal efficiency than OC at nominal and advanced spark timing, respectively.

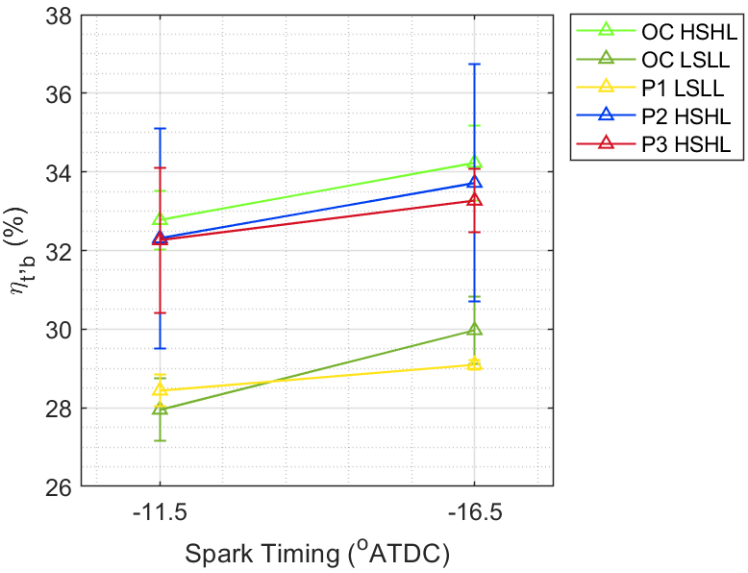

Figure 44: Brake thermal efficiency ($\eta_{t,b}$) at -11.5 and -16.5 °ATDC spark timings for OC and PCCs at varying speed and load.

Though P2 and P3 at nominal spark timing and OC at HSHL and advanced spark timing had similar combustion phasing, the test conditions had an even larger spread in brake thermal efficiency. P2 and P3 at nominal spark timing were both 1.97% less

efficient than OC at HSHL and advanced spark timing (Figure 44). Thus, at similar combustion phases, the Eco-Jet prechambers were less efficient than standard OC operation, producing less work per released fuel chemical energy.

OC at LSLL had a brake thermal efficiency of 27.95% at nominal spark timing and 29.97% at advanced spark timing, while P1 had a brake thermal efficiency of 28.44% at nominal spark timing and 29.10% at advanced spark timing. Thus, P1 was 0.49 percentage points higher in brake thermal efficiency than OC at LSLL and nominal spark timing, but was 0.87 percentage points lower in brake thermal efficiency at advanced spark timing. At nominal spark timing, P1 was able to produce more work per fuel chemical energy, but at advanced spark timing the OC engine operation improved in stability and efficiency and achieved higher brake thermal efficiency than P1. All PCCs were, on average, less efficient than the OC configuration. The design of each PCC (i.e. L/D ratio, β, and C_t) did not allow for proper mixing or ignition to operate as intended. In the pressure curves, the PCC cycles have higher peak pressures, which result in lower pressures at the end of expansion (Figure 31). Lower pressures at the end of expansion are attributed to earlier combustion phasing, contributing to high peak pressure, and enabling the fuel's energy to experience more of the expansion stroke. Thus, blowdown is different and may be affecting how the fuel is being combusted in each cycle. Additionally, earlier combustion phasing was expected to increase thermal efficiency because of the longer effective expansion stroke, though thermal efficiency was actually low. The low thermal efficiency may have been affected by heat losses caused by

additional water cooling of the PCCs or the higher temperatures from the PCC jets into the main chamber.

4.7. Emissions

4.7.1. Brake Specific Oxides of Nitrogen ($BSNO_x$)

Brake specific calculations evaluated engine emissions relative to how much useful work was produced by the engine, which provided a more complete accounting for emissions. Emissions are more accurately evaluated when comparing LSLL cycles to HSHL cycles through these brake specific quantities. Figure 45 shows $BSNO_x$ trends for the different experiments. For LSLL, P1 had $BSNO_x$ levels of 15.7 g/hp-hr and 14.6 g/hp-hr at nominal and advanced spark timing, respectively. OC at LSLL had $BSNO_x$ levels of 0.536 g/hp-hr and 0.521 g/hp-hr at nominal and advanced spark timing, respectively. Thus, OC at LSLL decreased $BSNO_x$ emissions by 96.6% at nominal spark timing and 96.4% at advanced spark timing when removing P1 and operating with OC. P1 had high NO_x concentrations due to increased temperatures in the cylinder and increased fuel consumption due to a poor mixing process.

P2 and P3 had $BSNO_x$ levels of 6.11 g/hp-hr and 7.30 g/hp-hr at nominal spark timing, respectively, and 5.37 g/hp-hr and 7.62 g/hp-hr at advanced spark timing, respectively. OC at HSHL had $BSNO_x$ levels of 2.94 g/hp-hr at nominal spark timing and 2.80 g/hp-hr at advanced spark timing. Thus, OC at HSHL had 51.9% and 59.7% lower $BSNO_x$ emissions at nominal spark timing than P2 and P3, respectively, and 47.9% and 63.3% lower $BSNO_x$ emissions than P2 and P3 at advanced spark timing, respectively.

Using the Eco-Jet prechambers increased $BSNO_x$ levels at both spark timings due to their inefficient design, resulting in poor ignition and a poor mixing process. Fuel consumption increased and IMEP stayed relatively constant when switching from OC to PCC operation, requiring the engine to consume more fuel to produce the same amount of work. In addition, P2 and P3 increased in-cylinder temperatures and pressures, which contributed to NO_x production and higher $BSNO_x$. Of the two Eco-Jet prechambers, P2 had lower $BSNO_x$ levels than P3.

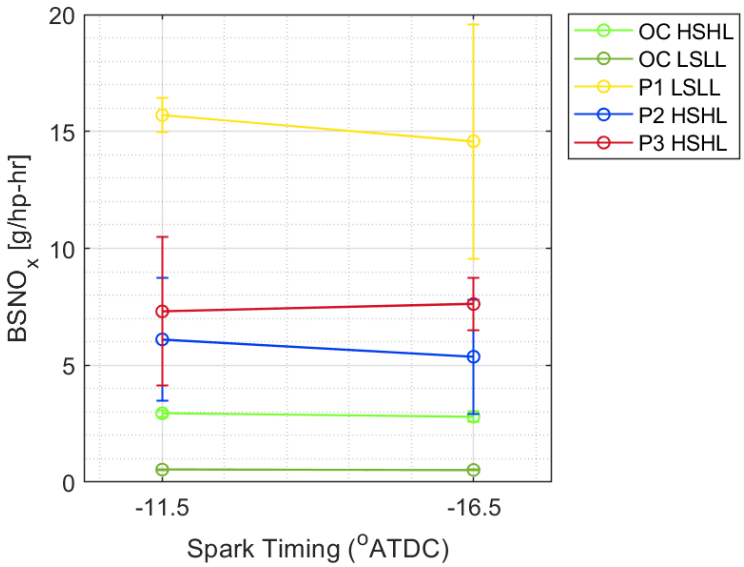

Figure 45: $BSNO_x$ at -11.5 and -16.5 °ATDC spark timings for OC and PCCs at varying speed and load.

The prechambers have much higher emissions than OC operation at HSHL or LSLL due to poor mixing, poor ignition, and higher pressure cycles. In addition, the fuel supply system does not have a uniform pressure entering both the MCC and PCC, with pressures fluctuating around ±20%. More importantly, the L/D ratios and Craya-Curtet

numbers of the PCCs tested in this thesis did meet minimum PCC performance standards, which resulted in poor mixing and ignition. Slefarski et al. found that with an improved fuel supply system and the addition of adequately designed prechamber technology in the GMVH-12 engine, NO_x emissions were reduced up to 60% [55]. With an alternate PCC design that is better matched for the Ajax E-565, reduction in $BSNO_x$ can be realized.

4.7.2. Brake Specific Total Hydrocarbons (BSTHC)

P1 had 65.2 g/hp-hr BSTHC at nominal spark timing and 56.9 g/hp-hr BSTHC at advanced spark timing (Figure 46). OC at LSLL had 76.0% and 61.3% lower BSTHC emissions than P1 at nominal and advanced spark timing, respectively. BSTHC decreased by 12.8% for P1 with advanced spark timing, while BSTHC increased by 40.6% with OC at LSLL with advanced spark timing. With advanced spark timing, P1 had fewer unburned hydrocarbons being short-circuited from the intake to the exhaust due to increased engine stability (Figure 35). The overall increase in THC emissions when using PCCs can also be attributed to the four-stroking phenomenon that occurred. P1 had much higher unburned hydrocarbons released in the exhaust compared to operating the engine with an OC configuration at LSLL due to a poor mixing system and poor ignition. OC experienced increased levels of BSTHC with advanced spark timing because more unburned hydrocarbons were short-circuited to the exhaust due to decreased engine stability.

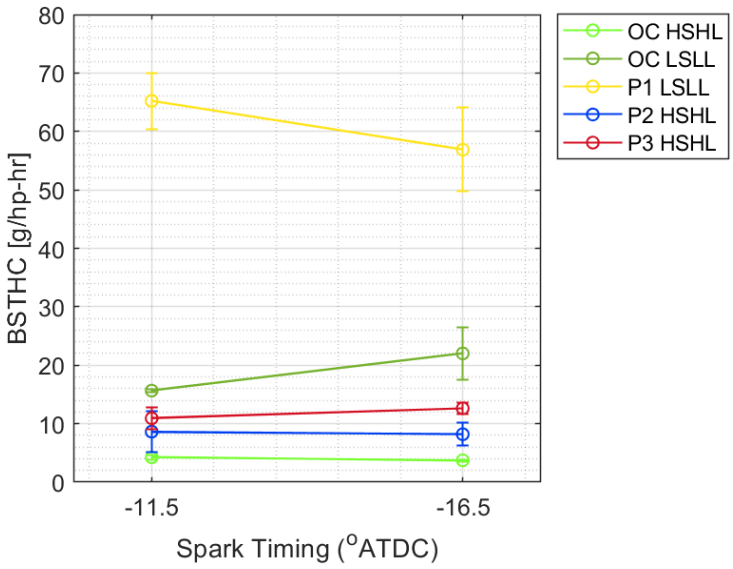

Figure 46: BSTHC at -11.5 and -16.5 °ATDC spark timings for OC and PCCs at varying speed and load.

P2, P3, and OC at HSHL all decreased engine stability with advanced spark timing (Figure 35), but P3 had a 15.8% increase in BSTHC from 10.9 g/hp-hr to 12.62 g/hp-hr while BSTHC for P2 and OC decreased by 5.11% and 12.0%, respectively, with advanced spark timing. BSTHC for the OC configuration was lower than P2 and P3 by 50.8% and 61.1% at nominal spark timing and lower by 54.4% and 70.4% at advanced spark timing, respectively. Similar to P1, BSTHC increased in both P2 and P3 due to a poor mixing process, poor ignition, an unoptimized swirling fuel supply, and unstable inlet pressure into the PCC and MCC.

4.7.3. Brake Specific Carbon Monoxide (BSCO)

The range of uncertainty at nominal spark timing did not provide a clear understanding of BSCO for each test condition, so a trend in BSCO cannot be determined.

However, BSCO at advanced spark timing can be assessed with reasonable certainty. P3 had a BSCO of 1.85 g/hp-hr at advanced spark timing, and OC at HSHL had a BSCO of 1.10 g/hp-hr, which was 40.5% lower than P3. P2 had an uncertainty that overlapped OC at HSHL with a similar BSCO level. At -16.5 °ATDC, P1 had a BSCO of 1.65 g/hp-hr, which was 20.9% less than OC at LSLL (Figure 47). Thus, P1 was more effective at reducing BSCO than OC at LSLL, while P2 and P3 appeared to have higher BSCO levels than OC at HSHL. A possible explanation for this is OC at LSLL had more incomplete reactions to form CO_2, resulting with more CO products [8]. BSCO for P1 was expected to be higher because engine stability was worse than under OC operation, and P1 consumed more fuel than OC at LSLL (Figure 37). P2 and P3 consumed more fuel than OC at HSHL and was less stable, resulting with higher levels of CO.

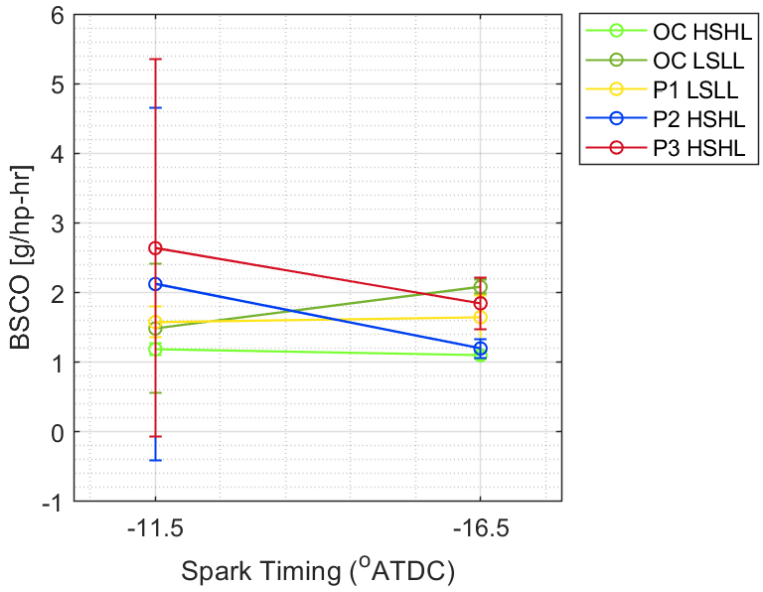

Figure 47: BSCO at -11.5 and -16.5 °ATDC spark timings for OC and PCCs at varying speed and load.

4.7.4. Brake Specific Carbon Dioxide ($BSCO_2$)

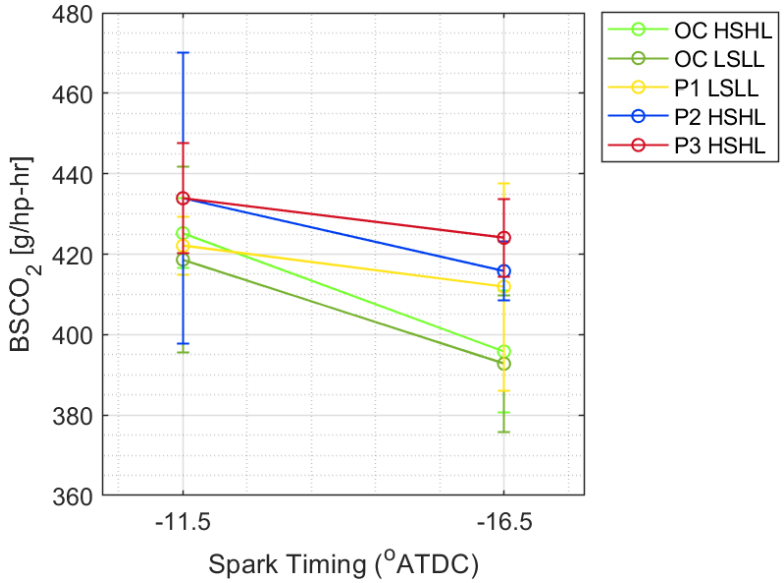

Figure 48: $BSCO_2$ at -11.5 and -16.5 °ATDC spark timings for OC and PCCs at varying speed and load.

Similar to BSCO, $BSCO_2$ had large ranges of uncertainty at both nominal and advanced spark timings, making it difficult to identify any clear trends. $BSCO_2$ does appear to decrease, on average, with advanced spark timing (Figure 48). A decrease in CO_2 concentration was expected with advanced spark timing as less fuel was introduced into the mixture, resulting in fewer complete reactions to form CO_2 [8]. P3 and OC at HSHL does not have overlapping uncertainty, which allowed for a clear indication that $BSCO_2$ was higher for P3 by 6.67% than operating the engine with an OC configuration at HSHL.

4.7.5. Brake Specific Oxygen (BSO_2)

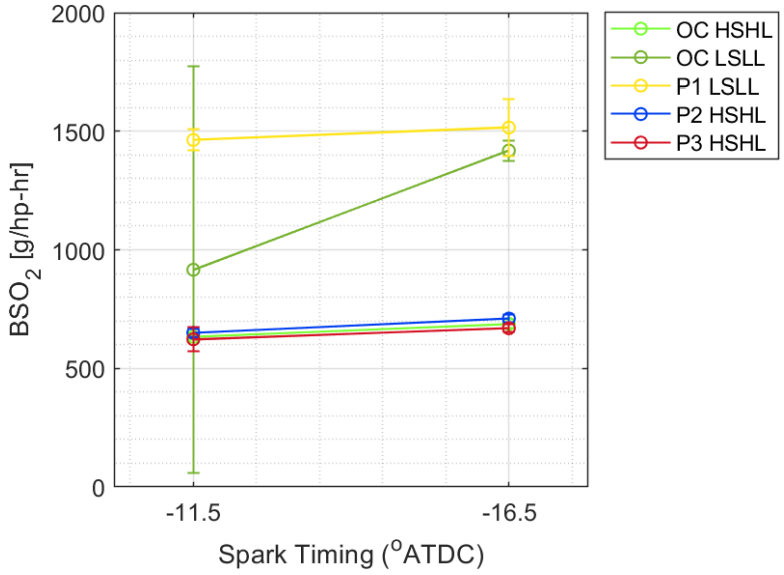

Figure 49: BSO_2 at -11.5 and -16.5 °ATDC spark timings for OC and PCCs at varying speed and load.

Despite the large uncertainty in OC at LSLL and nominal spark timing, BSO_2 had an increasing trend with advanced spark timing for all test conditions (Figure 49). An increasing trend in BSO_2 validated the decreasing trend in $BSCO_2$, as advancing the spark timing resulted with fewer complete reactions to form CO_2, which left more exhausted O_2. P1, P2, and OC at HSHL had similar levels and rises BSO_2, which corresponded to the decrease $BSCO_2$ showed in Figure 48. Despite the uncertainty in OC at LSLL and nominal spark timing, P1 and OC at LSLL appeared to have a similar rise in BSO_2, which corresponded to a decrease in $BSCO_2$ at advanced spark timing.

5. FUTURE WORK

The SIP and Eco-Jet prechambers used in this study should be redesigned (or new prechambers should be tested) to meet the following criteria in order to improve the mixing system and ignition: a Craya-Curtet number of about 0.3 [35], a Beta of 0.41 [37], a clearance volume of 2% [4], and an L/D ratio of at least 1.5 [4]. In addition, the fuel supply system should optimize fuel swirl, and pressure fluctuations at the inlet of the PCC and MCC should be kept to a minimum. Once the previous criteria are met, it would be valuable to complete the same experiments in this study, but with the addition of retarded spark timing if attainable, to measure the changes in engine performance and emissions to optimize PCC design and engine operation.

The current PCC fuel line incorporated the existing ethanol blending system, so future experiments should incorporate fuel blending to measure the effects on greenhouse gas emissions. Additionally, the present study tested the prechambers with the NGK Iridium WR5IX spark plug for P2 and P3 and the Champion W18 spark plug for P1. Changing spark plugs and measuring the effects on PCC ignition can be used to improve PCC ignition. The effect of nozzle design on PCC performance and emissions would also be interesting for experimentation as different nozzle sizes and arrangements have been shown to improve efficiency and reduce emissions in other natural gas engines [4]. In addition, changing orifice sizes to modify fuel metering via the PCC's check valve can be tested. Lastly, boosting the Ajax E-565 may further stabilize combustion and engine operation while achieving lower NO_x levels [4].

6. CONCLUSIONS

Prechamber technology can improve efficiency and reduce emissions in natural gas engines with the proper design. In the present study, the three prechambers tested, a standard SIP and two Eco-Jets, were designed with low Craya-Curtet numbers and length to diameter ratios. As a result, all of the prechambers experienced a poor mixing process and poor ignition. In addition, the Ajax E-565 operated with approximately a ±20% pressure fluctuation at the PCC and MCC inlet, which reduced engine efficiency, and the fuel supply system did not operate with an optimized fuel swirl pattern.

Operating the engine with the present PCCs resulted in up to 9.50% more fuel consumption than with an OC configuration, and decreases of up to 4.78% in combustion efficiency and up to 1.97% in brake thermal efficiency. As a result, OC operation resulted in $BSNO_x$, BSTHC, BSCO, and $BSCO_2$ levels that were lower than operating a PCC configured Ajax E-565 by up to 63.3%, 76.0%, 40.5%, 6.67% respectively.

As global fossil CO_2 emissions increase, with the largest contribution to rising CO_2 levels from fossil fuel combustion (i.e. internal combustion engines) [5], and as the U.S. continues to increase its natural gas fuel consumption, the need to reduce greenhouse gas emissions becomes more prevalent. Prechamber technology has been shown to reduce greenhouse gas emissions [2] [3] [4] [55] with proper design and engine operation. This study highlighted the ramifications of applying prechamber designs to an engine platform outside of their intended scope. Adjusting fuel inlet pressures, fuel swirl, Craya-Curtet numbers, and L/D ratios should improve the emissions and performance of the next

generation of prechambers for the small gas compression engine segment in order to realize the promise of prechamber combustion.

REFERENCES

[1] "Monthly Energy Review, Table 1.3 and 10.1," U.S. Energy Information Administration, 2020.

[2] D. B. Olsen and J. M. Lisowski, "Prechamber NOx formation in low BMEP 2-stroke cycle natural gas engines," *Applied Thermal Engineering,* pp. 687 - 694, 2009.

[3] D. J. Simpson and D. B. Olsen, "Precombustion Chamber Design for Emissions Reduction from Large Bore NG Engines," *Journal of Engineering for Gas Turbines and Power,* vol. 132, 2010.

[4] D. B. Olsen, J. L. Adair and B. D. Willson, "Precombustion Chamber Design and Performance Studies for a Large Bore Natural Gas Engine," *ASME Internal Combustion Division 2005 Spring Technical Conference*, 2005.

[5] C. Le Quere, R. M. Andrew, P. Friedlingstein, S. Sitch and J. Hauck, "Global Carbon Budget 2018," *ESSD,* vol. 10, no. 4, 2018.

[6] R. K. Pachauri and L. A. Meyer, "ontribution of Work-ing Groups I, II and III to the Fifth Assessment Report of the Intergovern-mental Panel on Climate Change," *IPCC,* p. 151, 2014.

[7] S. Ashish, "Improving the Efficiency of Gas Engines using Pre-chamber Ignition," *Lund University*, 2015.

[8] J. B. Heywood, Internal Combustion Engines Fundamentals, McGraw-Hill, 1988.

[9] Ajax Products Group, "Description of AJAX Engines," Cameron Corporation, 1963.

[10] E. O. Reinbold, "The AT27GL: A continuing development of the Waukesha AT series engine," *ASME - ICE,* vol. 22, pp. 23 - 30, 1994.

[11] J. G. Speight, "Chapter 10 - Combustion of Hydrocarbons," in *Handbook of Industrial Hydrocarbon Processes,* Gulf Professional Publishing, 2011, pp. 355 - 393.

[12] A. H. Lefebvre, Gas Turbine Combustion, 2nd Ed., Philadelphia: Taylor & Francis, 1999.

[13] C. T. Bowman, "Kinetics of Pollutant Formation and Destruction in Combustion," *Prog. Energy Combust. Sci.,* vol. 1, pp. 33 - 45, 1975.

[14] G. A. Lavoie, J. B. Heywood and J. C. Keck, "Experimental and Theoretical Investigation of Nitric Oxide Formation in Internal Combustion Engines," *Combust. Sci. Technol.,* vol. 1, pp. 313 - 326, 1970.

[15] E. L. Merryman and A. Levy, "Nitrogen Oxide Formation in Flames: The Roles of NO2 and Fuel Nitrogen," *Proceedings of Fifteenth International Symposium on Combustion,* p. 1073, 1975.

[16] W. A. Daniel, "Flame Quenching at the Walls of an Internal Combustion Engine," *Symposium (International) on Combustion,* vol. 6, no. 1, pp. 886 - 894, 1957.

[17] R. E. Hicks, R. F. Probstein and J. C. Keck, "A Model of Quench Layer Entrainment During Blowdown and Exhaust of the Cylinder of an Internal Combustion Engine," *SAE Transactions,* vol. 84, pp. 1298 - 1311, 1975.

[18] W. K. Cheng, D. Hamrin, J. B. Heywood, S. Hochgreb, K. Min and M. Norris, "An Overview of Hydrocarbon Emissions Mechanisms in Spark-Ignition Engines," *SAE Technical Paper Series,* 1993.

[19] C. S. McEnally, L. D. Pfefferle, B. Atakan and K. Kohse-Hoinghaus, "Studies of aromatic hydrocarbon formation mechanisms in flames: Profress towards closing the fuel gap," *Progress in Energy and Combustion Science,* vol. 32, pp. 247 - 294, 2006.

[20] N. A. Chigier, "Pollution Formation and Destruction in Flames," *Prog. Energy Combust. Sci.,* vol. 1, pp. 3 - 15, 1975.

[21] L. Dondero and J. Goldemberg, "Environmental implications of converting light gas vehicles: the Brazilian experience," *Energy Policy,* pp. 1703 - 1708, 2005.

[22] T. Korakianitis, A. M. Namasivayam and R. J. Crookes, "Natural-gas fueled spark-ignition (SI) and compression-ignition (CI) engine performance and emissions," *Progress in Energy and Combustion Science,* pp. 1 - 24, 2010.

[23] P. Mello, G. Pelliza, R. Cataluna and R. da Silva, "Evaluation of the maximum horsepower of vehicles converted for use with natural gas fuel," *Fuel,* vol. 85, no. 14 - 15, pp. 2180 - 2186, 2006.

[24] T. Thurnheer, P. Soltic and P. D. Eggenschwiler, "SI engine fuelled with gasoline, methane, and methane/hydrogen blends: heat release and loss analysis," *International Journal of Hydrogen Energy,* pp. 2494 - 2503, 2009.

[25] F. Hagos, A. Aziz and S. Sulaiman, "Investigation of deposit formation in direct-injection spark-ignition engine powered on syngas," *Int. J. Automot. Technol.,* pp. 479 - 485, 2015.

[26] C. Arcoumanis, H. Flora, J. W. Kim and H. M. Xu, "Injection natural gas engine for light-duty applications," *International Conference on 21st Century Emissions Technology*, 2000.

[27] K. Zeng, Z. Huang, B. Liu, L. Liu, D. Jiang and Y. Ren, "Combustion characteristics of a direct-injection natural gas engine under various fuel injection timings," *Applied Thermal Engineering,* pp. 806 - 813, 2006.

[28] A. R. Aziz and R. Shahzad, "Combustion analysis of a CNG direct injection spark ignition engine," *Int. J. Automot. Mech. Eng.*, pp. 157 - 170, 2010.

[29] S. Aljamali, S. Abdullah, W. Wan Mahmood and Y. Ali, "The effect of injection timings on performance and emissions of compressed natural-gas direct injection engine," *J. Combust.*, 2016.

[30] G. T. Chala, A. Aziz and F. Y. Hagos, "Natural Gas Engine Technologies: Challenges and Energy Sustainability Issue," *Energies*, 2018.

[31] D. E. Iocco, "Retrofit Precombustion Chamber Helps Cut Engine NOx Emissions," *Pipeline and Gas Industry,* vol. 78, no. 10, pp. 41 - 46, 1995.

[32] J. W. Gingrich, D. B. Olsen, P. Puzinauskas and B. D. Willson, "Precombustion Chamber NOx Emission Contribution to an Industrial High-Speed, Natural Gas Engine," *Int. J. Engine Res.,* vol. 7, pp. 41 - 49, 2006.

[33] T. J. Callahan and J. T. Kubesh, "Contribution of prechamber combustion to engine CO and HC emissions," *Gas Machinery Conference,* 1997.

[34] J. M. Lisowski, D. B. Olsen and A. P. Yalin, "Visible flame imaging of prechamber initiated combustion in a large bore natural gas engine," *GMRC Gas Machinery Conference,* 2006.

[35] A. C. Anderson, T. N. Chen and W. T. Hutchens, "The development and application of design criteria for precombustion chambers on natural gas fueled engines," *ASME,* 1984.

[36] T. M. Sine and P. J. Reif, "An overview of lean-burn conversion for older Dresser-Rand engines," *ASME - ICE,* vol. 27, no. 4, pp. 77 - 84, 1996.

[37] H. Watson, E. Milkins and L. Goldsworthy, "Optimizing the spark ignition pre-chamber geometry including spark plug configuration for minimum NOx emissions and maximum efficiency," *Proceedings SAE,* vol. 1, pp. 1 - 13, 1982.

[38] "Screw-In-PreChamber testing using the E-42 engine," Cooper Machinery, 2010.

[39] P. D. Ronney, "Laser Versus Conventional Ignition of Flames," *Optical Engineering,* vol. 33, pp. 510 - 521, 1994.

[40] H. Zhu, X. Yu, L. Wang and M. Zheng, "Effect of Discharge Energy Distribution on Flame Kernal Development," *Internal Combustion Engine Division Fall Technical Conference,* 2020.

[41] W. P. Attard and P. Parsons, "Flame Kernel Development for a Spark Initiated Pre-Chamber Combustion System Capable of High Load, High Efficiency and Near Zero NOx Emissions," *SAE International,* 2010.

[42] "Ajax E-565 Gas Engine - Simple, Rugged, Dependable," Cameron, Oklahoma City, 2012.

[43] "Economical and Dependable Ajax," Cooper Industries, Inc., Corry, 1968.

[44] "119 Series Fuel Gas Valve," Emerson Process Management Regulator Technologies, Inc., McKinney, TX, 2017.

[45] "NGI-1000 Generation Four Advanced Digital Ignition System for Small and Medium-Sized Industrial Engines," Altronic, LLC, Girard, Ohio, 2017.

[46] "DEA150 Air Cooled Eddy Current Dynamometer," Taylor Dynomometer, 2015.

[47] "MEXA-7000 MCU Operation Instruction Manual," Horiba, Ltd., 2007.

[48] "CO/CO2 (HC, NO, N2O, SO2) Analyzer AIA-72X Series Instruction Manual," Horiba, Ltd., 2007.

[49] "O2 Analyzer MPA-720," Horiba, Ltd., 2002.

[50] "THC Analyzer FIA-725A," Horiba, Ltd., 2003.

[51] "NO / NOx Analyzer CLA-720MA," Horiba, Ltd., 2003.

[52] A. J. Martyr and M. A. Plint, "The Combustion Process and Combustion Analysis," *Engine Testing (Fourth Edition),* pp. 375 - 406, 2012.

[53] C. Depcik, T. Jacobs, J. Hagena and D. Assanis, "Instructional Use of a Single-Zone, Premixed Charge, Spark-Ignition Engine Heat Release Simulation," *International Journal of Mechanical Engineering Education,* vol. 35, no. 1, pp. 1 - 31, 2007.

[54] C. F. Taylor, The Internal Combustion Engine in Theory and Practice: Vol. 1 - 2nd Edition, Revised: Thermodynamics, Fluid Flow, Performance, The MIT Press, 1985.

[55] R. Slefarski, M. Golebiewski, P. Czyzewski, P. Grzymislawski and J. Wawrzyniak, "Analysis of Combustion Process in Industrial Gas," *Energies,* vol. 11, 2018.

[56] R. G. Prucka, T.-K. Lee, Z. Filipi and D. N. Assanis, "Turbulence Intensity Calculation from Cylinder Pressure Data in a High Degree of Freedom Spark-Ignition Engine," *SAE Technical Paper 2010-01-0175,* 2010.

APPENDIX A

AJAX E-565 NATURAL GAS COMPOSITION

ATMOS Energy - Mid-Tex / APT
Gas Measurement Services
5420 LBJ Freeway, Suite 1800

10/21/2019 9:50 PM
Mercer, Dannie

Chromatograph Report

from Contract Day 09/01/2019 to Contract Day 09/30/2019

Station ID: 0802931426
Analysis ID: 04016300
Analysis Name: HICKS DRY PLANT
Company Name: ATMOS ENERGY - MID TEX / APT

Effective Date	Sat. HV	As Del HV	Dry HV	Meas. HV	Water Content	Wobbe	Real Gravity	C1	C2	C3	IC4	NC4	IC5	NC5	C6	C7	C8	C9	C10	N2	CO2	O2	H2O	CO	H2S	H2	He
09/01/2019 09:00	982.2	0.0	999.7	0.0		1309.5	0.5828	94.9089	2.1985	0.1146	0.0039	0.0077	0.0013	0.0011	0.0000	0.0000	0.0000	0.0000	0.0000	1.9421	0.8219	0.0000	0.0000	0.0000	0.0000	0.0000	0.0000
09/02/2019 09:00	983.3	0.0	1000.8	0.0		1313.8	0.5803	95.3719	2.0298	0.0914	0.0036	0.0062	0.0012	0.0009	0.0000	0.0000	0.0000	0.0000	0.0000	1.7381	0.7569	0.0000	0.0000	0.0000	0.0000	0.0000	0.0000
09/03/2019 09:00	984.1	0.0	1001.6	0.0		1314.4	0.5807	95.3807	2.0453	0.1034	0.0048	0.0079	0.0015	0.0011	0.0000	0.0000	0.0000	0.0000	0.0000	1.6409	0.8145	0.0000	0.0000	0.0000	0.0000	0.0000	0.0000
09/04/2019 09:00	984.0	0.0	1001.5	0.0		1314.7	0.5803	95.4197	2.0326	0.0960	0.0043	0.0071	0.0014	0.0010	0.0000	0.0000	0.0000	0.0000	0.0000	1.6477	0.7901	0.0000	0.0000	0.0000	0.0000	0.0000	0.0000
09/05/2019 09:00	984.6	0.0	1002.1	0.0		1313.9	0.5817	95.1315	2.1596	0.1396	0.0060	0.0105	0.0018	0.0014	0.0000	0.0000	0.0000	0.0000	0.0000	1.7876	0.7620	0.0000	0.0000	0.0000	0.0000	0.0000	0.0000
09/06/2019 09:00	985.1	0.0	1002.6	0.0		1314.0	0.5822	95.0352	2.2081	0.1587	0.0064	0.0122	0.0021	0.0018	0.0003	0.0003	0.0000	0.0000	0.0000	1.8379	0.7372	0.0000	0.0000	0.0000	0.0000	0.0000	0.0000
09/07/2019 09:00	984.2	0.0	1001.7	0.0		1313.5	0.5816	95.1191	2.1411	0.1374	0.0058	0.0118	0.0019	0.0017	0.0004	0.0004	0.0000	0.0000	0.0000	1.8522	0.7282	0.0000	0.0000	0.0000	0.0000	0.0000	0.0000
09/08/2019 09:00	984.1	0.0	1001.6	0.0		1312.7	0.5822	95.0475	2.1878	0.1315	0.0054	0.0114	0.0019	0.0016	0.0000	0.0000	0.0000	0.0000	0.0000	1.8240	0.7890	0.0000	0.0000	0.0000	0.0000	0.0000	0.0000
09/09/2019 09:00	985.4	0.0	1002.9	0.0		1314.0	0.5826	94.9902	2.2933	0.1304	0.0054	0.0113	0.0018	0.0016	0.0000	0.0000	0.0000	0.0000	0.0000	1.7665	0.7993	0.0000	0.0000	0.0000	0.0000	0.0000	0.0000
09/10/2019 09:00	984.9	0.0	1002.4	0.0		1312.5	0.5833	94.9007	2.3170	0.1331	0.0060	0.0103	0.0017	0.0014	0.0000	0.0000	0.0000	0.0000	0.0000	1.7821	0.8477	0.0000	0.0000	0.0000	0.0000	0.0000	0.0000
09/11/2019 09:00	986.4	0.0	1004.0	0.0		1314.6	0.5833	94.8873	2.3904	0.1479	0.0061	0.0109	0.0016	0.0012	0.0000	0.0000	0.0000	0.0000	0.0000	1.7325	0.8221	0.0000	0.0000	0.0000	0.0000	0.0000	0.0000
09/12/2019 09:00	984.4	0.0	1001.9	0.0		1313.3	0.5820	95.0682	2.2118	0.1228	0.0054	0.0098	0.0017	0.0014	0.0000	0.0000	0.0000	0.0000	0.0000	1.8090	0.7699	0.0000	0.0000	0.0000	0.0000	0.0000	0.0000
09/13/2019 09:00	985.9	0.0	1003.5	0.0		1315.1	0.5823	95.0261	2.3013	0.1362	0.0063	0.0100	0.0018	0.0014	0.0000	0.0000	0.0000	0.0000	0.0000	1.7509	0.7660	0.0000	0.0000	0.0000	0.0000	0.0000	0.0000
09/14/2019 09:00	983.5	0.0	1001.0	0.0		1313.0	0.5813	95.1957	2.0984	0.1128	0.0056	0.0089	0.0018	0.0015	0.0001	0.0001	0.0000	0.0000	0.0000	1.8137	0.7614	0.0000	0.0000	0.0000	0.0000	0.0000	0.0000
09/15/2019 09:00	983.8	0.0	1001.3	0.0		1313.3	0.5813	95.1995	2.1296	0.1085	0.0047	0.0070	0.0013	0.0010	0.0000	0.0000	0.0000	0.0000	0.0000	1.7737	0.7748	0.0000	0.0000	0.0000	0.0000	0.0000	0.0000
09/16/2019 09:00	984.5	0.0	1002.0	0.0		1313.9	0.5816	95.1273	2.2205	0.1030	0.0044	0.0064	0.0013	0.0009	0.0000	0.0000	0.0000	0.0000	0.0000	1.7658	0.7705	0.0000	0.0000	0.0000	0.0000	0.0000	0.0000
09/17/2019 09:00	985.6	0.0	1003.1	0.0		1315.4	0.5815	95.1223	2.2613	0.1119	0.0053	0.0087	0.0017	0.0014	0.0000	0.0000	0.0000	0.0000	0.0000	1.7571	0.7303	0.0000	0.0000	0.0000	0.0000	0.0000	0.0000
09/18/2019 09:00	983.9	0.0	1001.4	0.0		1313.7	0.5811	95.1421	2.1732	0.1040	0.0043	0.0079	0.0015	0.0013	0.0000	0.0000	0.0000	0.0000	0.0000	1.8692	0.6985	0.0000	0.0000	0.0000	0.0000	0.0000	0.0000
09/19/2019 09:00	984.0	0.0	1001.5	0.0		1313.5	0.5813	95.1912	2.1241	0.1167	0.0056	0.0093	0.0017	0.0015	0.0000	0.0000	0.0000	0.0000	0.0000	1.7887	0.7612	0.0000	0.0000	0.0000	0.0000	0.0000	0.0000
09/20/2019 09:00	985.5	0.0	1003.0	0.0		1315.6	0.5812	95.2430	2.1677	0.1244	0.0058	0.0095	0.0017	0.0014	0.0000	0.0000	0.0000	0.0000	0.0000	1.6754	0.7711	0.0000	0.0000	0.0000	0.0000	0.0000	0.0000
09/21/2019 09:00	983.9	0.0	1001.4	0.0		1312.6	0.5821	95.0037	2.2615	0.1021	0.0038	0.0050	0.0009	0.0005	0.0000	0.0000	0.0000	0.0000	0.0000	1.8538	0.7688	0.0000	0.0000	0.0000	0.0000	0.0000	0.0000
09/22/2019 09:00	984.0	0.0	1001.5	0.0		1313.9	0.5810	95.1995	2.1569	0.0969	0.0044	0.0065	0.0013	0.0010	0.0000	0.0000	0.0000	0.0000	0.0000	1.8020	0.7315	0.0000	0.0000	0.0000	0.0000	0.0000	0.0000
09/23/2019 09:00	984.5	0.0	1002.0	0.0		1314.3	0.5812	95.0992	2.2077	0.1142	0.0056	0.0094	0.0019	0.0015	0.0000	0.0000	0.0000	0.0000	0.0000	1.8951	0.6634	0.0000	0.0000	0.0000	0.0000	0.0000	0.0000
09/24/2019 09:00	985.5	0.0	1003.0	0.0		1315.1	0.5817	95.0238	2.2853	0.1274	0.0062	0.0112	0.0021	0.0017	0.0000	0.0000	0.0000	0.0000	0.0000	1.8818	0.6606	0.0000	0.0000	0.0000	0.0000	0.0000	0.0000
09/25/2019 09:00	985.0	0.0	1002.5	0.0		1314.9	0.5813	95.1816	2.1814	0.1169	0.0066	0.0113	0.0023	0.0019	0.0001	0.0001	0.0000	0.0000	0.0000	1.7616	0.7361	0.0000	0.0000	0.0000	0.0000	0.0000	0.0000
09/26/2019 09:00	986.5	0.0	1004.1	0.0		1316.2	0.5820	94.9962	2.3319	0.1452	0.0064	0.0133	0.0024	0.0022	0.0001	0.0001	0.0000	0.0000	0.0000	1.8358	0.6665	0.0000	0.0000	0.0000	0.0000	0.0000	0.0000
09/27/2019 09:00	988.3	0.0	1005.9	0.0		1317.7	0.5827	94.8855	2.4014	0.1755	0.0102	0.0269	0.0052	0.0052	0.0014	0.0014	0.0000	0.0000	0.0000	1.8720	0.6155	0.0000	0.0000	0.0000	0.0000	0.0000	0.0000
09/28/2019 09:00	988.2	0.0	1005.8	0.0		1318.8	0.5817	95.1610	2.2668	0.1540	0.0115	0.0256	0.0054	0.0051	0.0014	0.0014	0.0000	0.0000	0.0000	1.6970	0.6707	0.0000	0.0000	0.0000	0.0000	0.0000	0.0000
09/29/2019 09:00	985.3	0.0	1002.8	0.0		1315.8	0.5808	95.1819	2.1859	0.1204	0.0064	0.0134	0.0026	0.0024	0.0003	0.0003	0.0000	0.0000	0.0000	1.8462	0.6403	0.0000	0.0000	0.0000	0.0000	0.0000	0.0000
09/30/2019 09:00	987.3	0.0	1004.9	0.0		1317.9	0.5815	95.1169	2.2521	0.1597	0.0094	0.0216	0.0043	0.0040	0.0008	0.0008	0.0000	0.0000	0.0000	1.8124	0.6181	0.0000	0.0000	0.0000	0.0000	0.0000	0.0000
Flow Weighted Average:	984.9	0.0	1002.4	0.0			0.5817	95.1112	2.2066	0.1243	0.0058	0.0109	0.0020	0.0017	0.0001	0.0001	0.0000	0.0000	0.0000	1.7952	0.7420	0.0000	0.0000	0.0000	0.0000	0.0000	0.0000